



# Mapping of Compositional Diversity and Chronological Ages of Lunar Farside Multiring Mare Moscoviense Basin: Implications to the Middle Imbrian Mare Basalts

A. Karthi<sup>1</sup>, S. Arivazhagan<sup>1</sup>, and Manish Sharma<sup>2</sup>

<sup>1</sup> Centre for Applied Geology, The Gandhigram Rural Institute—Deemed to be University, Gandhigram, Dindigul- 624302, Tamil Nadu, India; [arivusv@gmail.com](mailto:arivusv@gmail.com)

<sup>2</sup> College of Natural and Health Sciences, Zayed University, P.O. Box 144534, Abu Dhabi, United Arab Emirates; [Manish.Sharma@zu.ac.ae](mailto:Manish.Sharma@zu.ac.ae)

Received 2022 June 7; revised 2022 August 22; accepted 2022 August 31; published 2022 November 11

## Abstract

The Mare Moscoviense is an astonishing rare flatland multi-ring basin and one of the recognizable mare regions on the Moon's farside. The mineralogical, chronological, topographical and morphological studies of the maria surface of the Moon provide a primary understanding of the origin and evolution of the mare provinces. In this study, the Chandrayaan-1 M<sup>3</sup> data have been employed to prepare optical maturity index, FeO and TiO<sup>2</sup> concentration, and standard band ratio map to detect the mafic indexes like olivine and pyroxene minerals. The crater size frequency distribution method has been applied to LROC WAC data to obtain the absolute model ages of the Moscoviense basin. The four geological unit ages were observed as 3.57 Ga (U-2), 3.65 Ga (U-1), 3.8 Ga (U-3) and 3.92 Ga (U-4), which could have been formed between the Imbrian and Nectarian epochs. The M<sup>3</sup> imaging and reflectance spectral parameters were used to reveal the minerals like pyroxene, olivine, ilmenite, plagioclase, orthopyroxene-olivine-spinel lithology, and olivine-pyroxene mixtures present in the gabbroic basalt, anorthositic and massive ilmenite rocks, and validated with the existing database. The results show that the Moscoviense basin is dominated by intermediate TiO<sup>2</sup> basalts that derived from olivine-ilmenite-pyroxene cumulate depths ranging from 200 to 500 km between 3.5 Ga and 3.6 Ga.

*Key words:* astrobiology – molecular processes – methods: data analysis – techniques: image processing – techniques: imaging spectroscopy – techniques: spectroscopic – planets and satellites: composition – planets and satellites: surfaces – planets and satellites: terrestrial planets

## 1. Introduction

The Moon is the closest celestial body to Earth, with a presence of abundant resources that are key to understanding the origin and evolution of the Earth-Moon system and the solar system (Jaumann et al. 2012). The Moon was generated by massive melting of a magma ocean process from the surface to a certain depth, followed by the formation of first-order lunar structure and stratification of crust, mantle and most likely the core (Shearer & Papike 1999, 2005). During the global differentiation processes, the prehistoric lunar crust was formed by the flotation of plagioclase composition. Subsequently, through impact-induced magmatism or volcanism, the subsurface mantle derivatives collected early mafic cumulates in the crust (Wood et al. 1970; Warren 1985; Shearer & Papike 1999, 2005). Several studies show that during its early stratification, the lunar interior underwent major reorganization. The crystallization of the lunar magma ocean (LMO) produced the stratification sequence of the different compositions that have been observed from several numerical models, in sequential combinations of the compositions; olivine > orthopyroxene±olivine > olivine + clinopyroxene ± plagioclase > clinopyroxene + plagioclase > clinopyroxene +

plagioclase + ilmenite (Snyder et al. 1992; Shearer et al. 2006; Elardo et al. 2011).

The lunar surface has a variety of igneous rocks such as ferroan anorthosite, Mg-rich rocks, and potassium (K), rare-earth elements (REE) and phosphorus (P) (KREEP) rocks with varying chemical and mineral compositions, according to samples from the Apollo and Luna missions (Shearer et al. 2006). The interiors of impact basins were flooded with basalts and represent a secondary crust. The mare basalts were produced by decompression melting of the mantle cumulates that formed during the crystallization of the magma ocean. A majority of mare basalts erupted to the lunar surface in the interval between 3.1 and 3.9 Ga and covered around 17% of the lunar surface area (Shearer et al. 2006; Pieters et al. 2011; Qiao et al. 2021a).

There are 22 mare basins on the Moon, out of which 19 are located on the nearside, while the other three basins are located on the farside. The nearside and farside of the Moon are different in their geological aspects. The low albedo nearside of the Moon is dominated by basaltic mare deposits. In contrast, the bright highland deposits (anorthosite) are believed to be remnants of the Moon's original crust on the farside. All the

nearside basins have experienced mare volcanism and subsequent mare filling. However, only a few mare basins on the farside have undergone mare volcanism and infilled by mare deposits, which are very unusual compared to the nearside Moon's topography (Head 1976; Thaisen et al. 2011). The farside has a few mare basins such as Orientale, Moscoviense, and Ingenii. The surface of Mare Moscoviense shows flattened mare deposits, whereas the nearest to the rim of the basin (inner ring) contains the feldspathic assemblages. This part of the mare associated highland locations may still contain ample evidence for the original flotation of crust and secondary petrogenesis associated with the LMO concept (Smith et al. 1970; Wood et al. 1970; Warren 1985; Thaisen et al. 2011). Interpreting the recent lunar mission's high spatial and spectral resolution data has revealed an overall understanding of the origin and evolution of lunar surfaces (Jolliff 2006; Kumar et al. 2009; Ouyang et al. 2010; Pieters et al. 2011; Thaisen et al. 2011; Arivazhagan & Karthi 2018; Howari et al. 2021; Howari et al. 2022).

The Moscoviense basin exhibits strong mare deposits that are considered as a window to the mantle source due to its thin crust on the Moon's farside (Pike & Spudis 1987; Craddock et al. 1997; Pieters et al. 2011; Thaisen et al. 2011; Calzada & Mest 2013; Hess et al. 2020; Meng et al. 2020; Mikolajewski et al. 2021). Therefore, Mare Moscoviense is the appropriate location from the farside to investigate the evolutionary history of the mare emplacement and its compositional variations. The prime aim of the present work is to do a comprehensive analysis of compositional, chronological and topographical studies of the Moscoviense basin by using various lunar remote sensing data sets to comprehend the evolutionary history of the mare basalts.

## 2. Study Area

The multi-ring impact basin of Mare Moscoviense (Sea of Muscovy—27.3°N 147.9°E) is situated on the farside of the Moon within the Feldspathic Highland Terrain (FHT), covering an area of about 445 km in diameter (Thaisen et al. 2011; Bhatt et al. 2018; Mikolajewski et al. 2021). Moscoviense is one of the important and noteworthy mare-filled basins that holds significant records of the mare volcanism and provides facts about the crypto maria concept as well (Thaisen et al. 2011; Bhatt et al. 2018). The location map of the study area is displayed in Figure 1. The basin's three-dimensional (3D) topographic map and cross-section are prepared using Lunar Reconnaissance Orbiter Camera (LROC) Wide Angle Camera (WAC) Digital Terrain Model (DTM) data as depicted in Figure 2(i) and (ii). The slope map of the Mare Moscoviense basin is shown Figure 3.

## 3. Geological Units of Mare Moscoviense

The major geological units of Mare Moscoviense basin consist of different units such as Upper Imbrian Mare Unit

(Im2-flat and smooth surface, old basaltic lava deposit), Plains Unit (Ip-intermediate albedo, Imbrain or older units and INp—comprises moderate to high density of superposed craters), Crater Undivided Unit (Ic-younger impact materials from a primary impact), Crater Unit (Nc-Nectarian epoch, muted morphology, primary impact event materials), Lower Crater Unit (Ic1-major impact source material, younger than Imbrium assemblage), Terra Unit (Nt-diverse age of superposed craters, moderate coarse terrain), Basin Undivided Unit (pNb-degraded morphology, primary impact materials and Nb-Nectarian age, mostly with impact related structures), Crater Fracture Floor Unit (Icf-Imbrian epoch, fractured or brittle material lifted and prolonged) and Basin Massif Unit (pNbm- Pre-Nectarian unit, large hilly landforms) (Wilhelms et al. 1987; Fortezzo et al. 2020). The geological map of the Mare Moscoviense basin is featured in Figure 4. The Moscoviense basin geology map is obtained from the new “Unified Geologic Map” of the Moon (1:5M, 2020) (Fortezzo et al. 2020), and their characteristics and spatial coverage are discussed in Table 1.

## 4. Datasets

The Moon Mineralogy Mapper ( $M^3$ ), a visible and near-infrared (400–3000 nm) imaging spectrometer, was a guest instrument on the Chandrayaan-1 (Ch-1) mission, which was designed to operate in two modes. The optimal mode has a spatial resolution of 70 m pixel<sup>-1</sup> and a spectral resolution of 10 nm with 260 bands, whereas the global mode includes 85 bands with a spectral range of 460–3000 nm (20–40 nm) and a spatial resolution of 140 or 280 m pixel<sup>-1</sup> (Goswami & Annadurai 2009). In this study, Ch-1  $M^3$  global mode photometrically calibrated reflectance hyperspectral data that were downloaded from the orbital data explorer-planetary data system (ODE-PDS) node. The  $M^3$  data, trimmed from 540–2500 nm to avoid stretching of the plot resulting in high reflectances at longer wavelengths due to thermal emission (Kramer et al. 2011), were used to investigate the compositional diversity of the Mare Moscoviense basin. For the chronological and topographical analysis, images from the Lunar Reconnaissance Orbiter (LRO)—LROC-WAC-100M and DTM-100M (Stoffler et al. 2006; Robinson et al. 2010) were used. The geological characteristics of the Moscoviense have been displayed using the Unified Geologic Map of the Moon (1:5M, Fortezzo et al. 2020) acquired from the Astropedia USGS portal. The compositional spectra obtained from Ch-1  $M^3$  were validated using the Reflectance Experiment Laboratory (RELAB) rocks and minerals spectral database.

## 5. Methods

### 5.1. Standard Band Ratio (SBR)

The standard band ratio (SBR) is an important approach for distinguishing different lithological characteristics on the lunar

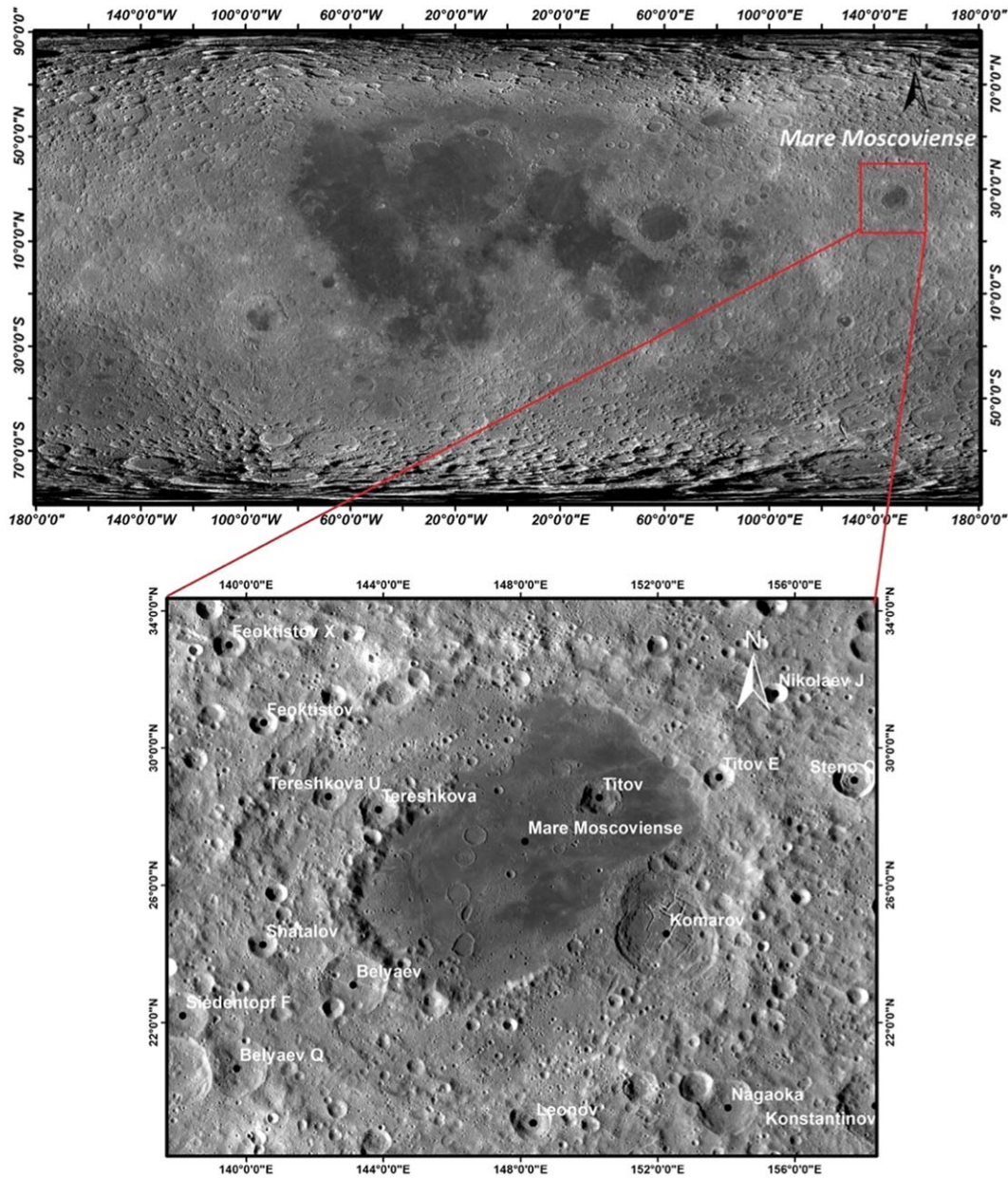


Figure 1. Location map of Mare Moscoviense (LROC-WAC) images with resolution  $100 \text{ m pixel}^{-1}$ .

surface. Using Clementine data, Lucey et al. (1998) and Lucey et al. (2000a, 2000b) produced several ratio combinations for distinguishing lithological variances on the lunar surface. The SBR approach was utilized by Arivazhagan & Anbazhagan (2012); Arivazhagan & Karthi (2018) and Karthi & Arivazhagan (2022) to differentiate the diverse lithologies of the Apollo 17 landing area, Mare Crisium basin and Mare Orientale basin, respectively. To differentiate distinct lithologies in the basin,  $M^3$  data have been utilized to produce the SBR map using band combinations of R-750 nm/540 nm, G-750/950 nm and

B-540 nm/750 nm. Figure 5(A) and (B) depicts the SBR map and respective unit spectral profiles of the Moscoviense basin.

### 5.2. Optical Maturity (OMAT) Mapping

The optical properties of lunar soils have been altered as a result of meteoritic impacts, solar wind and cosmic ray exposure, which affect the maturity of lunar soils (Lucey et al. 2000b; Grier et al. 2001). Due to space weathering, optical maturity induces reddening, darkening and band depth reductions (Jin et al. 2013). Grier et al. (2001) mapped

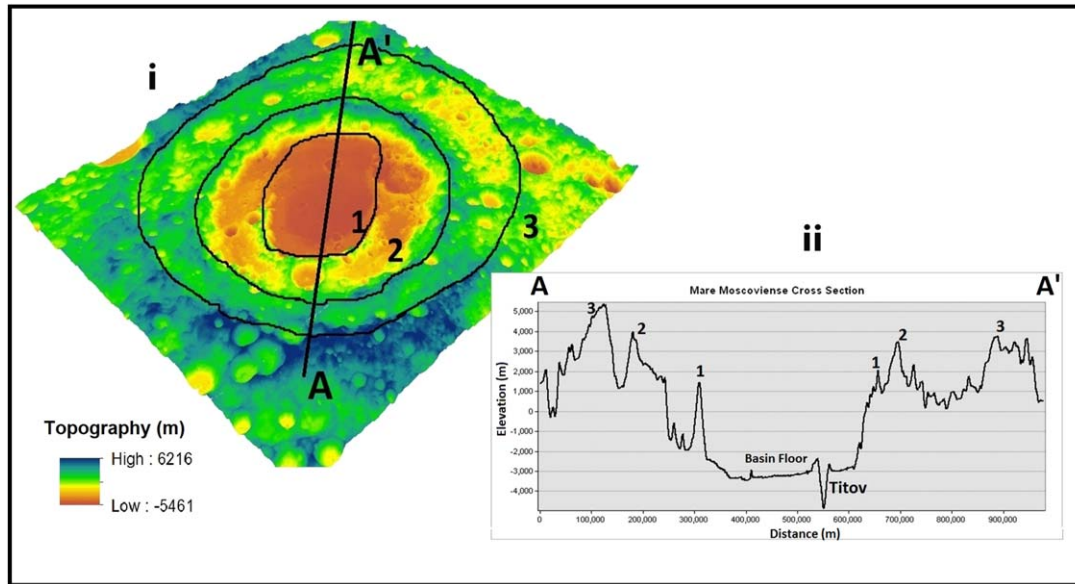


**Figure 2.** (i) The Mare Moscoviense topography map (3D) (LROC-WAC-DTM with 118 m spatial resolution). (ii) Cross section of the basin (A-A'). The black marked circles indicate the rings of the basin (1-inner ring-200 km, 2-middle ring-425 km and 3-outer ring-700 km).

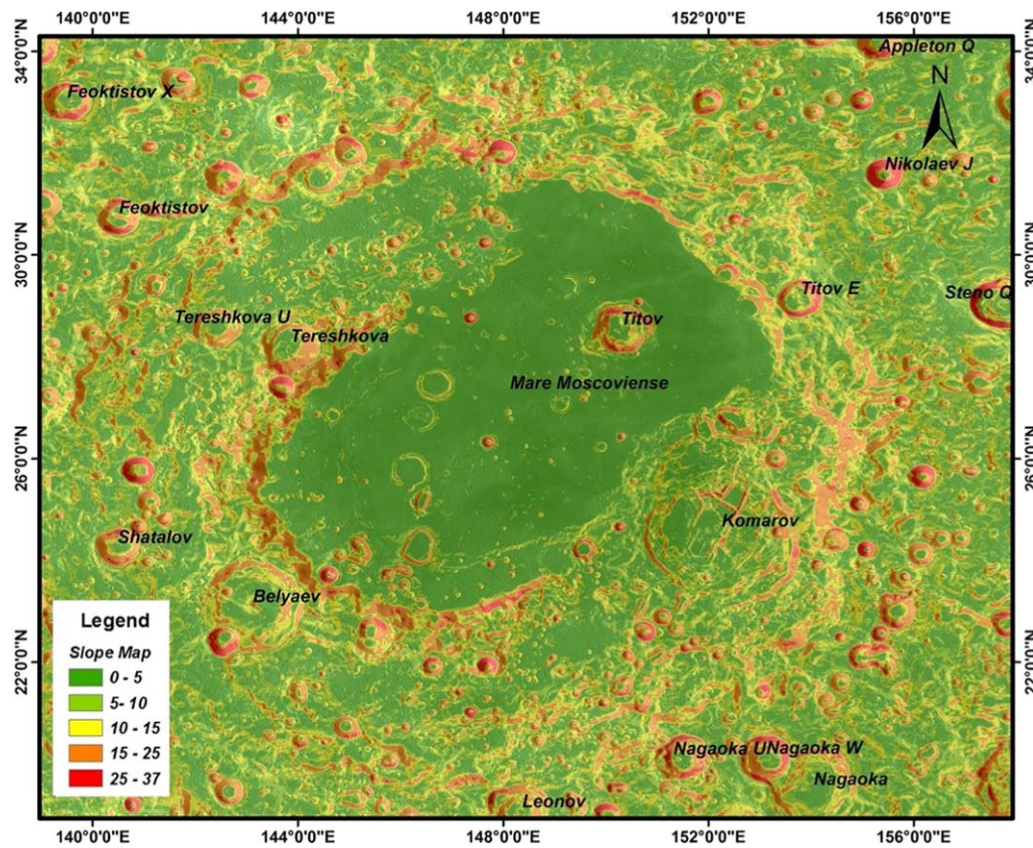


**Figure 3.** Slope map of the Mare Moscoviense basin.

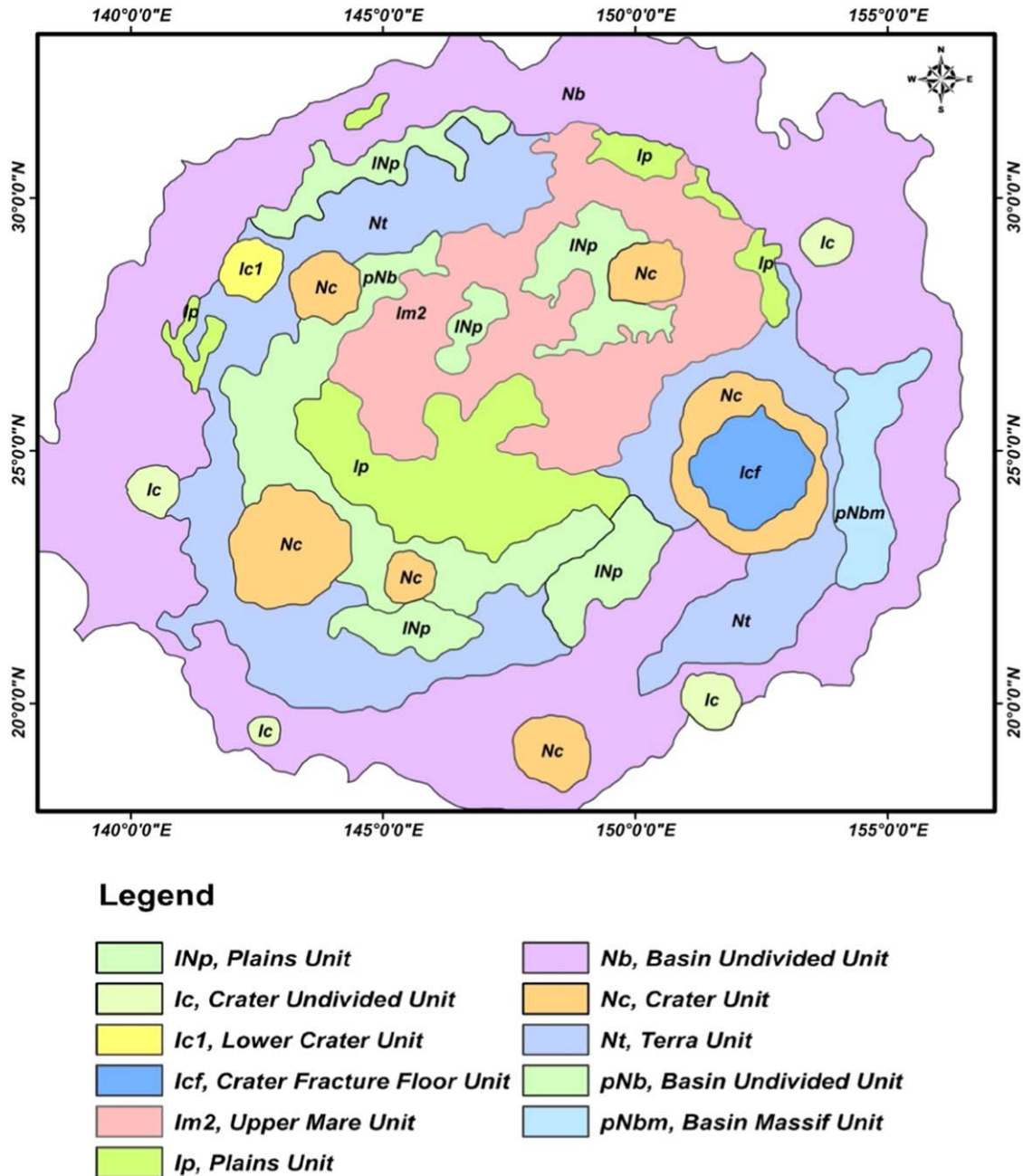


Figure 4. Geological map of Mare Moscoviense (Fortezzo et al. 2020).

the optical maturity of the lunar surface using a ratio of 750 nm and 950 nm from Clementine multispectral data. Bharti et al. (2014) used Ch-1 M<sup>3</sup> to study the optical maturity features of the lunar Mare Fecunditatis Naonobu crater. A high OMAT index suggests fresh surfaces (low maturity), whereas a low OMAT value indicates more mature surfaces (Jin et al. 2013). The maturity index and morphological characteristics of the Moscoviense basin were calculated using the Lucey et al.

(2000a, 2000b) parameter, as shown in Figure 6.

$$OMAT = ((R750 - 0.03)^2 + ((R950/R750) - 1.31)^2)^{1/2}, \quad (1)$$

where R750 is the reflectance at 750 nm and R950 is the reflectance at 950 nm.

The equation was created originally to analyze Clementine data. Additionally, the M<sup>3</sup> data are resampled to suit the

**Table 1**  
The Geological Units of the Mare Moscoviense Basin and their Interpretation

S. No	Unit symbol	Epoch	Unit Description	Surface Area (Km <sup>2</sup> )	Interpretation (Wilhelms et al. 1987; Fortezzo et al. 2020)
1.	Ic	Imbrian	Crater Undivided Unit	2702.5	Subdued topographic relief and morphology compared to younger impact features. Material from a primary impact event.
2.	Ic1	Imbrian	Lower Crater Unit	1076	Similar to Ic, subdued morphology and material from a primary impact event, younger than Imbrium group materials but older than Orientale group materials.
3.	INp	Imbrian-Nectarian	Plains Unit	13 002.4	Smooth, flat to undulating surface, moderate to high density of superposed craters. The formation of this material is possibly from the Imbrian and Nectarian units.
4.	Nc	Nectarian	Crater Unit	13 622.5	Subdued morphology and material from a primary impact event. The topographic relief compared to younger impact features, with broad flat floors typically another unit. Very little to no ejecta present.
5.	Ip	Imbrian	Plains Unit	14 253.6	Ambiguous origin, likely Orientale end other large impact crater ejecta. The intermediate albedo, smooth, flat to undulatory terrain.
6.	Nt	Nectarian	Terra Unit	32 820.8	A varied mixture of local erosional debris as well as crater and basin ejecta. Moderately rough surface, rolling to moderately rugged overall relief, with diverse ages of superposed and buried craters.
7.	pNb	Pre-Nectarian	Basin Undivided Unit	10 903.6	It is subdued and has eroded mountain rings, arcuate segments of rings, rim, walls and inner-ring materials.
8.	Nb	Nectarian	Basin Undivided Unit	77 844.3	Material slumped walls and blocks of basins, aggregates of closely spaced subdued hills and ridges. It has impact related structures and ejecta materials.
9.	Im2	Imbrian	Upper Mare Unit	23 461.6	Flattened, smooth surfaces, lower albedo and crater density, filled by basaltic lava flows.
10.	Icf	Imbrian	Crater Fracture Floor Unit	3634.3	Crater floors typically domed, with furrows, linear to curvilinear fractures with variable widths and depths. Blocks and material between the fractures sometimes reoriented.
11.	pNbms	Pre-Nectarian	Basin Massif Unit	4156.3	The uplifted bedrock structure formed during the formation of basins. Large mountainous landforms commonly lying along arc, both continuous and discontinuous, gradational with generally finer-scale topography.

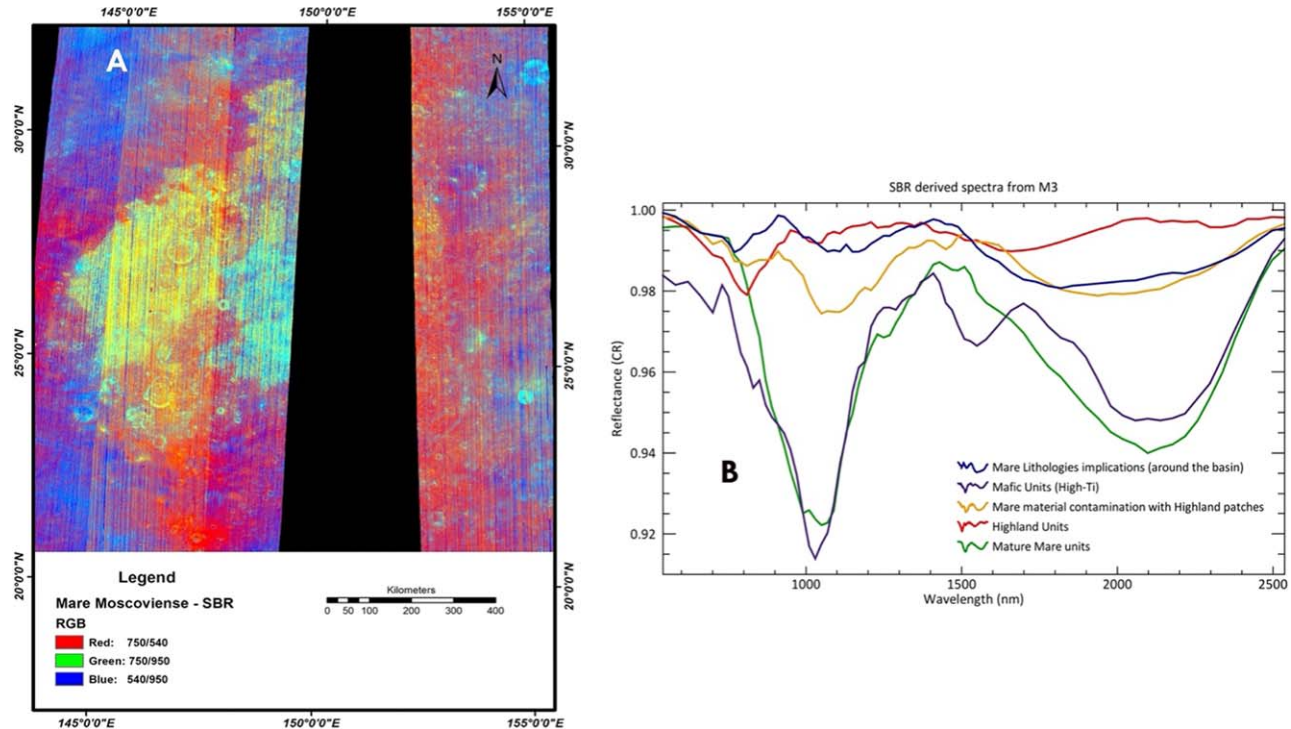


Figure 5. (A) The “SBR” image shows the various lithological patches over Mare Moscoviense. (B) Spectral profiles from each lithological character.

spectral grid of the Clementine instrument for more precision; furthermore, the interpolation algorithm indicates a difference of less than 1%. As a result, it is feasible to adapt Lucey’s model, which was initially developed for Clementine data to  $M^3$  data (Zhang et al. 2020).

### 5.3. FeO Mapping

Iron oxide in lunar soil provides information on petrologic and impact mixing processes that affect lunar material. Mapping the iron is important for comprehending the lunar mare areas (Blewett et al. 1997). Lucey et al. (1998, 2000a, 2000b) developed a technique for mapping lunar surface FeO utilizing Clementine ultraviolet/visible (UV/VIS) data reflectances at 750 nm and the 950 nm/750 nm ratio. Wu et al. (2012) used the Chang’e-1 Imaging Interferometer (IIM) to map the global FeO concentration. The parameters stated by Wu et al. (2012) were used on the 750 nm and 910 nm bands of  $M^3$ , which are closest to the Chang’e-1 IIM bands, to determine the FeO concentration of the Moscoviense basin in the current work. Figure 7 depicts the FeO concentration map of Mare Moscoviense.

$$\Theta_{\text{Fe}} = -\arctan((R_{910}/R_{750}) - 1.19/R_{750} - 0.08), \quad (2)$$

where  $R_{750}$  is the reflectance at 750 nm and  $R_{910}$  is the reflectance at 910 nm.

### 5.4. $\text{TiO}_2$ Mapping

Mapping the quantity of ilmenite ( $\text{FeTiO}_3$ ) in lunar mare basalts and soils is an essential component of lunar exploratory geological researches and prospective resource usage sources for lunar oxygen (Allen et al. 1994; Ling et al. 2011). The  $\text{TiO}_2$  content distribution of mare deposits is consistent with their source regions (mare cumulates), the cumulate from the LMO coupled with dynamic sinking and dense mixing of Ti-rich, Fe-rich late-stage cumulates finally rising as Mg-rich early cumulates or undifferentiated rock (Dowty 1975; Herbert 1980; Ryder 1991; Hess & Parmentier 1995; Giguere et al. 2000). Chemically, the mare basalts may be split into two classes. Specifically, (1) the younger, low-Ti group (3150–3450 Ma, 1%–5% wt.  $\text{TiO}_2$ ), and (2) the older, high-Ti group (3550–3850 Ma, 9%–13% wt.  $\text{TiO}_2$ ) (Papike et al. 1976). Giguere et al. (2000) classified the lunar basalts as Very Low—1.0%, Low—1.0%–4.5%, Intermediate—4.5%–7.5%, High—7.5%–10% and Very High—10%–13% based on  $\text{TiO}_2$  ranges. Charette et al. (1974) created the first Ti elemental concentration map from mature mare soils by correlating the UV/VIS spectral ratio, and this approach was then used and refined by others (Blewett et al. 1997; Lucey et al. 1998, 2000a, 2000b). The  $\text{TiO}_2$  content of the Mare Moscoviense basin was mapped in this work utilizing the Ling et al. (2011) parameter that was altered and applied on the 540 nm and 750 nm bands. Figure 8

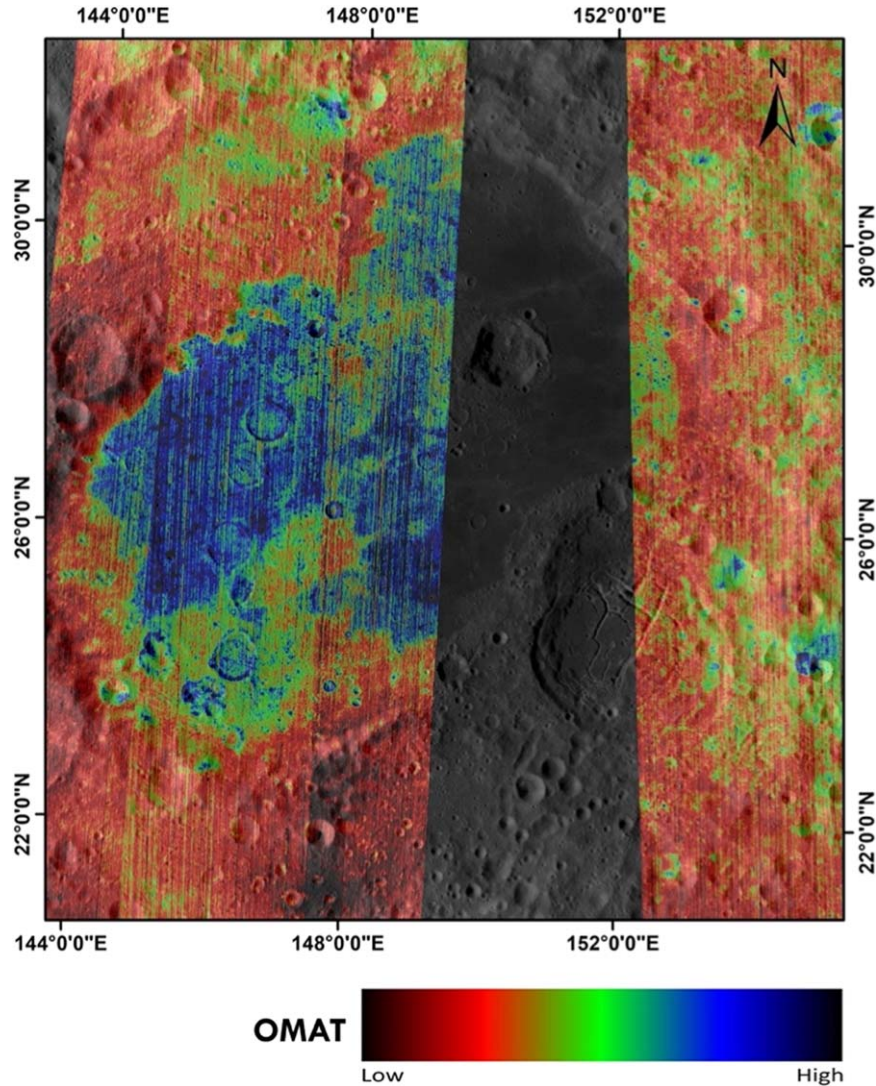


**Figure 6.** The optical maturity map of Mare Moscoviense overlaid on the LROC-WAC image.

depicts the  $\text{TiO}_2$  map of the Moscoviense basin.

$$\Theta_{\text{Ti}} = \arctan(R_{540}/R_{750} - 0.531/R_{750} - 0.061), \quad (3)$$

where  $R_{540}$  is the reflectance at 540 nm and  $R_{750}$  is the reflectance at 750 nm.

### 5.5. $1 \mu\text{m}$ and $2 \mu\text{m}$ IBD Mapping

Absorption features of  $1 \mu\text{m}$  and  $2 \mu\text{m}$  are the primary resources for evaluating lunar surface mineralogy, particularly for mafic minerals like olivine and pyroxenes (Burns 1993; Isaacson et al. 2013; Arivazhagan & Karthi 2018; Salem et al. 2022). The Integrated Band Depth (IBD) defines the band depths of absorption characteristics at  $1 \mu\text{m}$  and  $2 \mu\text{m}$  to distinguish spectral differences related with mafic minerals, soil maturity and space weathering (Mustard et al. 2011). The IBD

spectral parameters of  $1 \mu\text{m}$  and  $2 \mu\text{m}$  were used in the Copernicus crater on the Moon to map the olivine exposures using Clementine data (Le Mouélic 2001). The  $\text{M}^3$  and related ground truth data (RELAB) were used to map the distribution of mafic minerals like “olivine” and “pyroxene” on the lunar surface in Copernicus, Aristarchus, Marius and Naonobu craters, and northern Mare Imbrium, northeastern Oceanus Procellarum, Mare Crisium and Mare Orientale basins (Isaacson et al. 2011; Klima et al. 2011; Mustard et al. 2011; Qiao et al. 2014; Bharti et al. 2014; Arivazhagan & Karthi 2018; Qiao et al. 2021b; Karthi & Arivazhagan 2022). In the present study, the  $1 \mu\text{m}$  IBD was processed by using 789 nm to 1308 nm spectral bands in the 20 nm interval to map the mafic lithologies, whereas  $2 \mu\text{m}$  IBD was measured using 1658 nm to 2457 nm spectral bands at 40 nm intervals to detect

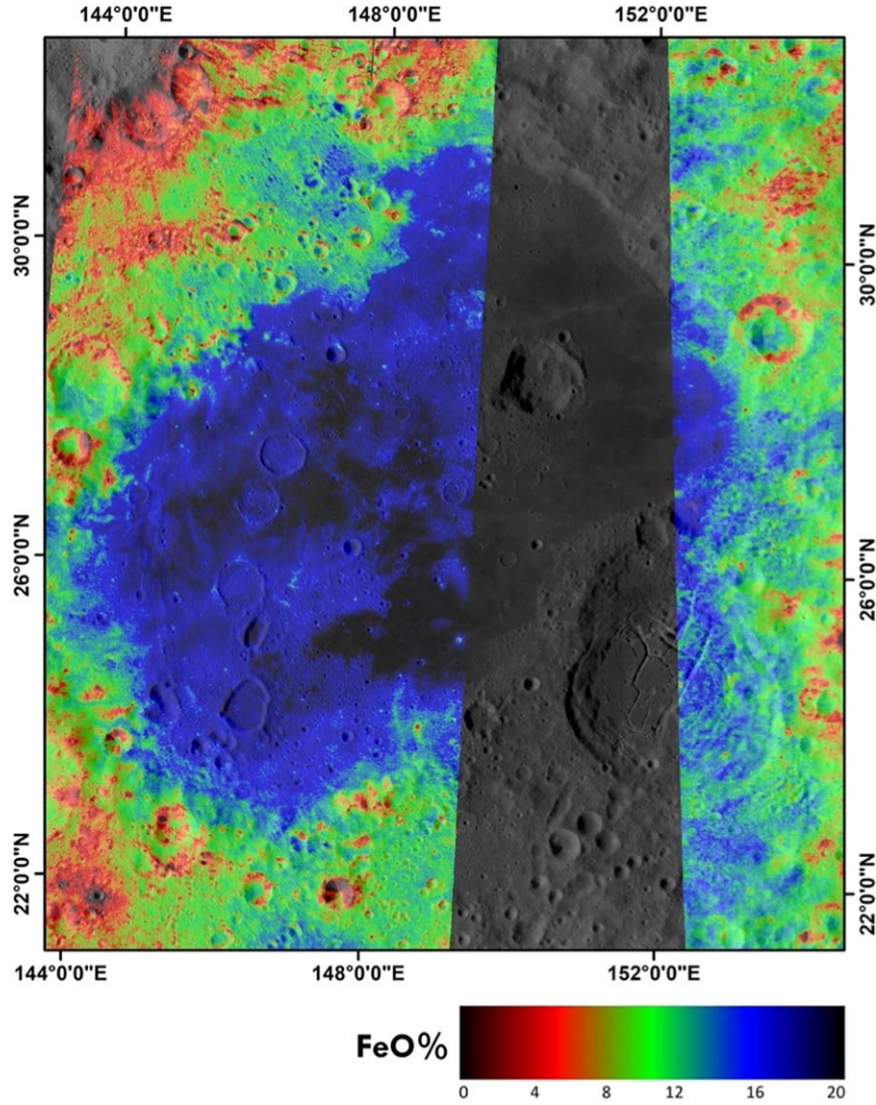


**Figure 7.** The FeO map of Mare Moscoviense overlaid on an LROC-WAC image.

the calcic pyroxene-rich zones, as shown in Figure 9(B). The typical spectra produced from the  $1\ \mu\text{m}$  and  $2\ \mu\text{m}$  IBDs for the validation are depicted in Figure 9(C)(i)–(iii). The following  $1\ \mu\text{m}$  and  $2\ \mu\text{m}$  band depth algorithms were adopted from Isaacson et al. (2011); Klima et al. (2011).

$$\begin{aligned}
 &1\ \mu\text{m band depth} \\
 &= \sum_{n=0}^{26} 1 - R(789 + 20n)/R_c(789 + 20n), \quad (4)
 \end{aligned}$$

$$\begin{aligned}
 &2\ \mu\text{m band depth} \\
 &= \sum_{n=0}^{21} 1 - R(1658 + 40n)/R_c(1658 + 40n), \quad (5)
 \end{aligned}$$

where  $R$  refers to the reflectance at a given wavelength, and  $R_c$  is the continuum reflectance defined as a straight line across the absorption band.

### 5.6. Chronological Investigation

Impact cratering is a typical geological event on the solid bodies of our solar system. In general, this procedure is used to determine the relative ages of planetary surfaces (Michael & Neukum 2010). Recent planetary missions give high-resolution remote sensing data for many planets, allowing scientists to build crater catalogs with their chronological dates (Stepinski et al. 2012; Atheer et al. 2016; Robbins 2016, 2018; Howari et al. 2022). To calculate the absolute age of

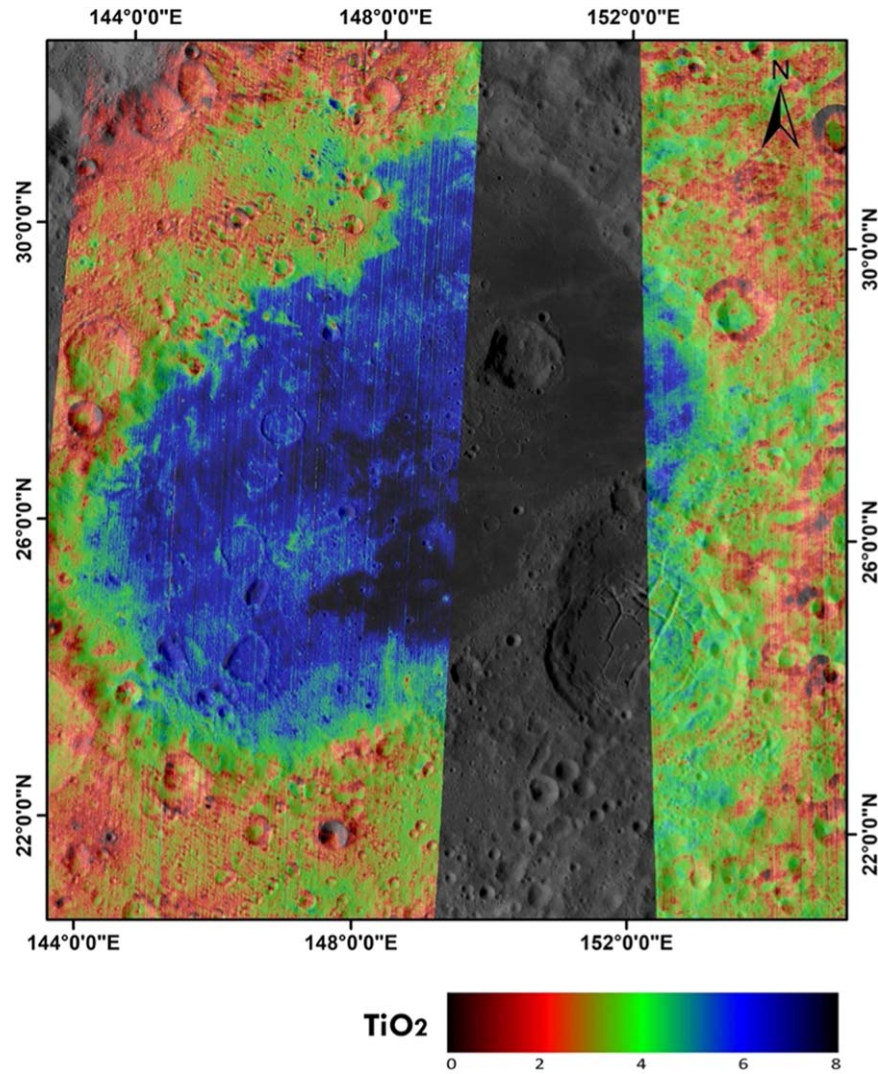


**Figure 8.** The  $\text{TiO}_2$  map of Mare Moscoviense overlaid on the LROC-WAC image.

planetary bodies, a single unified technique for analyzing impact craters and estimating their diameters has been created. To determine the age from remote sensing data, most chronological studies of a planetary surface use a well-developed and recognized statistical approach that is called “crater size frequency distribution” (CSFD). Traditionally, many academics estimate the CSFD by manually counting craters and determining sizes of the craters to highlight the ages of the craters using satellite imagery (Kneissl et al. 2011; Michael and Neukum 2010; Qiao et al. 2014; Atheer et al. 2016; Arivazhagan & Karthi 2018; Qiao et al. 2021c; Howari et al. 2021; Karthi & Arivazhagan 2022).

Several tools have been created to aid in manual crater counting, such as the CraterTools program developed by Kneissl et al. (2011) to label craters on planetary surface bodies. Michael & Neukum (2010) created the CraterStats

software tool, which aids in estimating the surface’s “absolute model ages” (AMA). The geological borders of the Moscoviense basin (interior) have been separated into four units (Unit 1–4) for the purpose of studying chronological variations, as illustrated in Figure 10. In the current study, craters with diameters ranging from 20 m to 18 km were collected using ArcGIS crater tools, and the ages of the units were determined using IDL integrated tool crater stats. The estimated age of the different units of the basin is given in Table 2.

### 5.7. Mineralogical Investigation of Moscoviense Features

Lunar morphology has always been an important part of lunar exploration (Ouyang 2005). The current status of the mare areas may be directly given by morphological feature-based compositional mapping of the lunar surface, which can

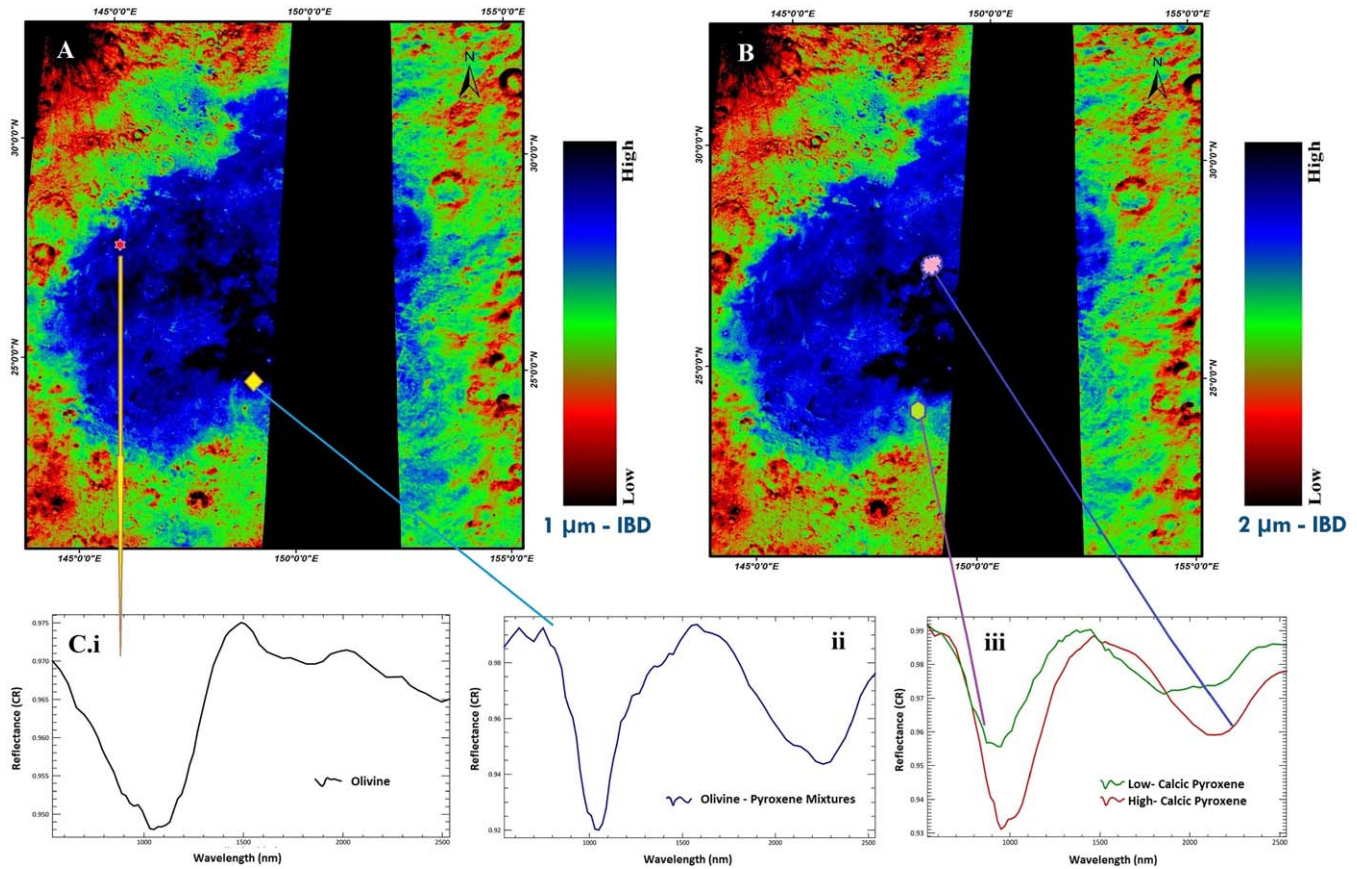


**Figure 9.** (A) The  $1 \mu\text{m}$  IBD map. (B)  $2 \mu\text{m}$  IBD map. (C)(i) Spectra of olivine, (ii) spectra of olivine-pyroxene mixtures and (iii) the pyroxene spectral characters.

**Table 2**  
The AMA of Mare Moscoviense from LROC-WAC

S.No	Name of the Units	Age of the Unit (Geological units based)	Craters counted	Surface area ( $\text{km}^2$ )	LROC—WAC (our results)	Error (Ga)
1	Unit—1	Imbrian (light plains)	292	13,195	3.65 Ga	+0.018/−0.020
2	Unit—2	Imbrian	669	23,486	3.57 Ga	+0.045/−0.064
3	Unit—3	Nectarian with Imbrian age	234	4,810	3.8 Ga	+0.02/−0.03
4	Unit—4	Nectarian	61	1,437	3.92 Ga	+0.026/−0.032

provide the genesis and evolution history of the mare basins. The Mare Moscoviense basin has a ray crater, swirls, wrinkle ridges and a few unidentified or suspected craters (Isaacson et al. 2011; Thaisen et al. 2011). Figure 11 depicts selected morphological aspects of the Mare Moscoviense basin. A ray crater is located on the basin's western rim, near highland pits, implying that partial highland materials tainted with mare patches are on the crater and the ray occurrence zone (Isaacson et al. 2011) (Figure 11(A)). The swirls are found in the western part of the Mare Moscoviense basin and extend for several tens of kilometers with a linear, jagged or curvilinear appearance (Lunar Swirls-Lroc.asu website I). They are also expressed as

albedo differences on the surface that are associated with wrinkle ridges (Wilhelms et al. 1987; Richmond et al. 2005; Blewett et al. 2011; Thaisen et al. 2011) (Figure 11(B)). The wrinkle ridges developed on the basin floor parallel to the northeast scarp, perpendicular to the length of the mare toward its midway and along an arc in the southwest section of the mare; these are all suggestive of basin floor subsidence and contraction (Lunar Wrinkle Ridge-Lroc.asu website II) (Gillis 1998; Yue et al. 2017) (Figure 11(C)). Three unnamed craters in the Moscoviense basin reveal the prevailing mare flow across the floor and around the craters (Robbins 2018 - Moon crater database) (Figure 11(D)). The ray crater, wrinkle ridges,

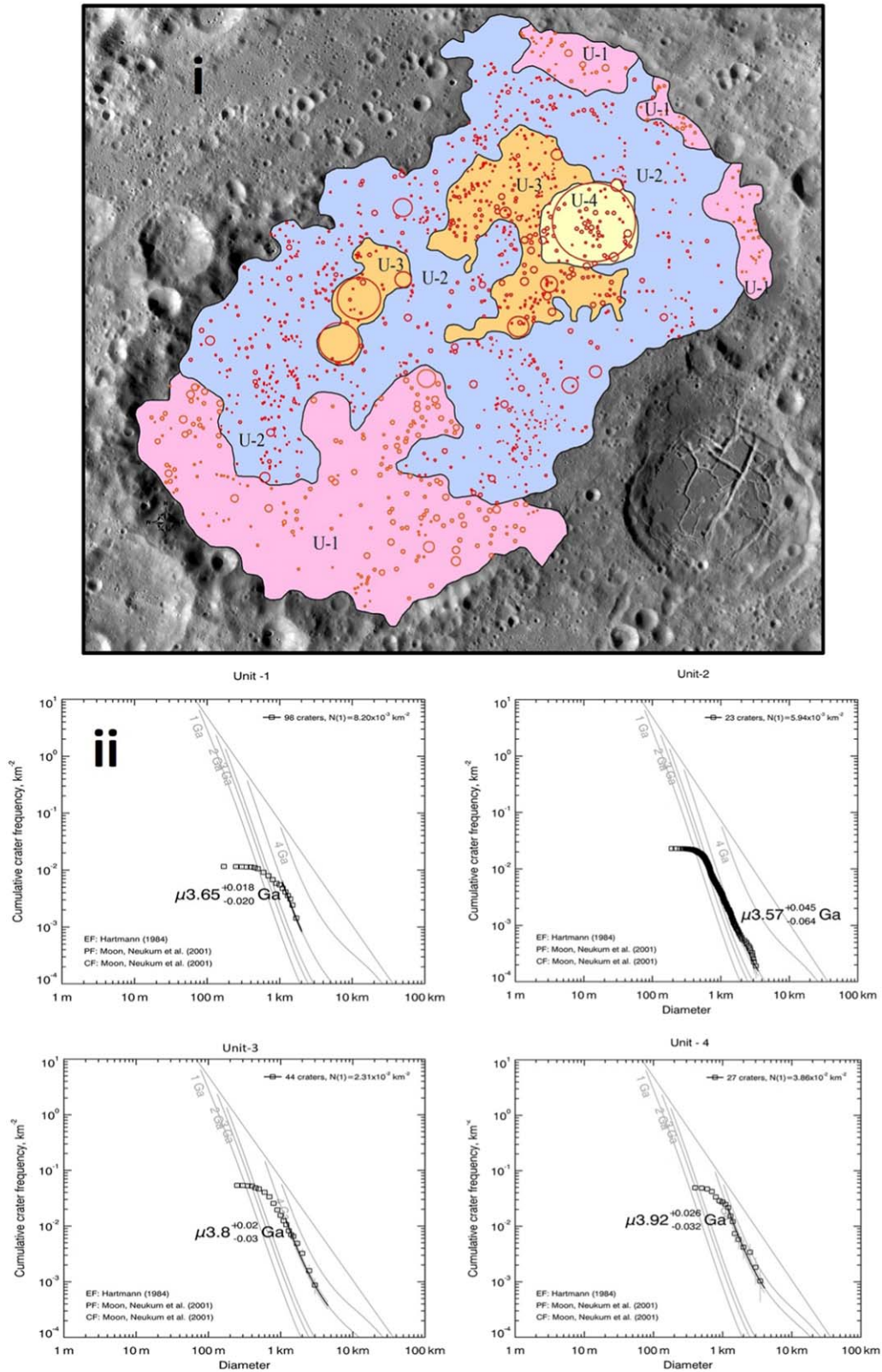


**Figure 10.** (i) The Mare Moscovense unit-based crater counted CSFD map. (ii) The crater counted unit ages of the Moscoviense (Unit 1—3.65 Ga, Unit 2—3.57 Ga, Unit 3—3.8 Ga and Unit 4—3.92 Ga).

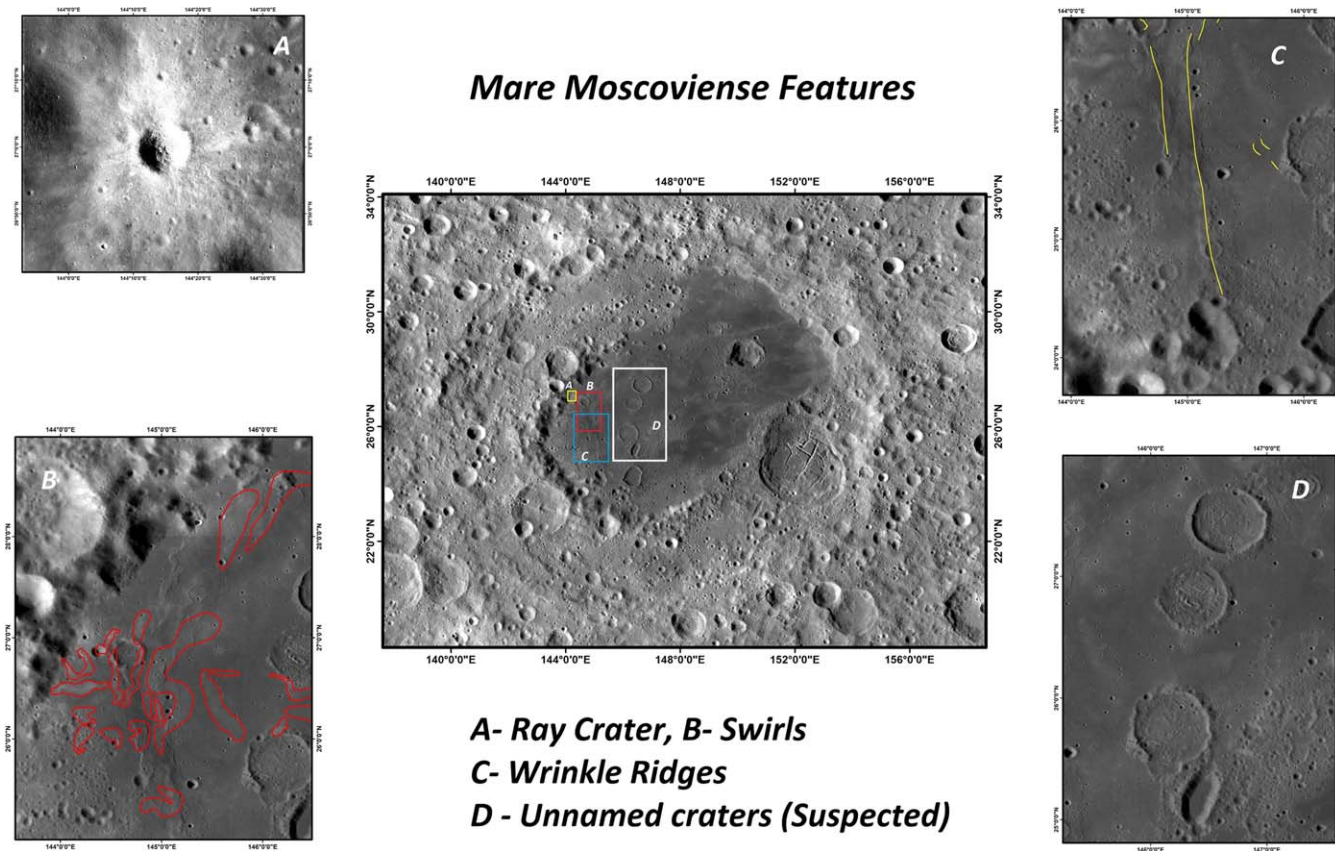


**Figure 11.** Selected morphological features of Moscoviense. (A) Ray crater, (B) swirls (outlined in red), (C) wrinkle ridges (marked in yellow lines) and (D) unnamed craters (suspected feature).

unnamed craters suspected (UCS) and swirls were studied to find the diverse mineralogical characteristics in the basin using the OMAT index, FeO and TiO<sub>2</sub> concentrations and spectral characterization.

## 6. Results and Discussions

### 6.1. Topographical Studies

Mare Moscoviense is occupied by a complete mare patch on the inner basin floor and rugged appearance in the eastern portion of the basin. Thaisen et al. (2011) and Mikolajewski et al. (2021) have stated that Mare Moscoviense has three distinct rings such as the inner ring, middle ring and outer ring (exterior ring). The present study’s 3D topographic image displays the three different rings of the basin that are clearly shown in Figure 2(i). The inner ring (1) diameter is 200 km, whereas the middle ring (2) and outer ring (3) have diameters of 425 km and 700 km, respectively (Figure 2(ii)). The Moscoviense basin has topography that includes a peak ring as well as rings that are offset to the southeast. These rings do not have the conventional concentric ring spacing seen in other basins, suggesting that they were created by an oblique impact

or maybe many impacts (Thaisen et al. 2011). The average depth of the basin is measured via cross-section (Figure 2(i)) as 5 km by using the LROC-WAC-DTM (Figure 2(ii)).

The surface slopes and their pattern in a given area could provide a vital clue to the morphological history of any planetary surface in terms of both genesis and evolution. The topographic slope characterization is valuable for framing and understanding the planetary landscape evolution processes (Sharpton & Head 1985; Kreslavsky & Head 1999; Aharonson et al. 2001; Rosenburg et al. 2011; Kreslavsky & Head 2016). The present study observed the entire basin slope as 0–37° using LROC-DTM data. The slope map of the Moscoviense, delineated by the slope patterns, has very high slope observed at crater walls (25°–37°), but low and moderate slope found on the basin floor (mare units) (Figure 3).

### 6.2. Mapping of SBR

The SBR map displays the color variants as yellow and orange representing the mature mare units and mare mixed highland materials, respectively (Figure 5(A)). The dark blue color indicates the highland composition. The cyan color shows

the high mafic index, whereas the red color exposes the highland materials (Figure 5(A)).

The spectral information collected based on the SBR is shown in Figure 5(B). For the present study, the  $M^3$  spectral profiles were characterized based on their symmetry, position, shape and depth of the systematic absorption characteristics by using full width at half maximum (FWHM) technique and validated with returned RELAB spectral information of the lunar samples (Burns 1993; Cloutis & Gaffey 1993; Anbazhagan & Arivazhagan 2009; Arivazhagan & Karthi 2018).

The mature mare units exhibit significant asymmetrical absorption at 1030 nm and broadening absorption at 2137 nm due to clinopyroxene (CPx), moderate plagioclase absorption at 1250 nm and moderate Ti-ilmenite absorption at 1458 nm, indicating a basaltic composition. Due to the  $Fe^{2+}$  electronic transition, two diagnostic absorption bands centered between 1000 nm and 2000 nm were identified in lunar pyroxenes. Ortho or low calcic pyroxene (OPx) has absorption band centers between 900 and 940 nm and 1850 nm to 1950 nm, whereas CPx exhibits two absorption bands near 950–1150 nm and 2000–2350 nm. Moreover, the pyroxenes contain Fe, Mg and Ca substitutions, and the systematic variations in absorption band centers are observed. Plagioclase feldspar has a high overall reflectance as well as 1250 nm absorption due to ferrous iron. Ilmenite exhibits moderate/broad absorption near 600–700 nm, a reflectance peak at 1000 nm, moderate broad absorption between 1200 and 1500 nm, and a significant reddening effect beyond 1700 nm (Reiner et al. 2009; Isaacson et al. 2011; Arivazhagan & Karthi 2018).

The mafic units exhibit modest  $Fe^{2+}$  absorption at 810 nm, significant asymmetrical absorption at 1010 nm, broad asymmetrical absorption at 2058 nm owing to CPx and moderate Ti-ilmenite absorption at 1489 nm, indicating basaltic composition (Figure 5(B)). The highland unit exhibits  $Fe^{2+}$  absorption around 800 nm, moderate plagioclase absorption near 1200 nm and moderate ilmenite absorption at 1548 nm, indicating anorthositic composition with ilmenite contamination (Charlier et al. 2015).

### 6.3. OMAT, FeO and TiO<sub>2</sub>

The darker zones of the central, southern and northern Moscoviense basin correspond to low maturity (blue color) (Figure 6), which indicates the mafic composition. The rim of the basin shows the high maturity (red color), representing the highland units like anorthositic compositions (Figure 6). The Moscoviense basin has an FeO concentration ranging up to 20% (Figure 7). FeO concentration <6% is noticed near the basin's rim, 7%–14% FeO concentration seen in the northern and southern regions of the basin, and 15%–20% FeO concentration reported in the middle and western portions of the basin (Figure 7).

The Moscoviense basin has a TiO<sub>2</sub> content up to 8% (Figure 8). The intermediate Ti-content (4.5%–7.5%) found in the basin's middle and southern regions indicates the presence of intermediary Ti basalts (blue) (Figure 8). The production of mare basalts with more than 5% TiO<sub>2</sub> might have entailed the mixing of early cumulates with late stage cumulates rich in clinopyroxene and ilmenite (Herbert 1980; Hess 1991; Hess & Parmentier 1995; Lucey et al. 1996; Giguere et al. 2000). Because ilmenite would not have achieved the saturation limit in the leftover liquid until >90% of the magma ocean had solidified, ilmenite-bearing cumulates would represent up to 5–10 vol percent of the lunar surface, possibly accounting for the scarcity of high-Ti mare basalts (Giguere et al. 2000).

The low Ti content (1%–4.5%) is reported at the northern, southern and western regions of the Moscoviense basin (near the rim). The mare basalts with less than 5 percent of TiO<sub>2</sub> created by partial melting of olivine and orthopyroxene cumulates have been experimentally synthesized by Longhi (1992). The fact that 80% of the mare basalts have <5 percent of TiO<sub>2</sub> is consistent with their genesis as partial melts from cumulates generated in the LMO. Low-Ti (1.0–4.5 wt percent TiO<sub>2</sub>) and Intermediate-Ti (4.5–7.5 wt% TiO<sub>2</sub>) mare accumulations are most abundant, revealing the aerial distribution of high Ti-basalts on the lunar surface decreases as TiO<sub>2</sub> percent increases, for instance, the High-Ti (>7.5 wt% TiO<sub>2</sub>) mare units constitute only 5% of the lunar maria (Dowty 1975; Hess 1991; Hess & Parmentier 1995; Lucey et al. 1996; Giguere et al. 2000). The Ti-concentration of the basin shows the dominant Intermediate Ti-basalts at the central portions of the Mare Moscoviense basin, which could have been derived from the age in between 3.5 to 3.6 Ga with source rocks of “olivine-ilmenite-pyroxene” cumulates piled at a depth of 200–500 km (Papike et al. 1976; Arivazhagan & Karthi 2018). This indicates that the basalts with intermediate TiO<sub>2</sub> levels might be more widespread than the high-Ti units (Giguere et al. 2000). Table 3 shows the Mare Moscoviense FeO and TiO<sub>2</sub> concentrations obtained from the present study (selective regions) and compares with previously published results.

### 6.4. 1 $\mu$ m and 2 $\mu$ m IBD

The blue color of the 1  $\mu$ m IBD indicates the high concentration of olivine and pyroxene found in the central, southern and western parts (Figure 9(A)). The 1  $\mu$ m band depth olivine features strong narrow spectral absorption at 1050 nm, and “olivine-pyroxene mixtures” (OPM) show absorption at 1050 nm and 2200 nm (Figure 9(C)(i) and (ii)). Olivine exhibits multiple component wide absorption about 1050 nm, and as the proportion increases, the absorption center shifts toward the higher wavelength. Beyond 1600 nm, both terrestrial and meteoritic olivine were shown to be featureless (Crown & Pieters 1987; Pieters & Englert 1997; Le Mouélic 2001). At 1050 nm, the OPM spectra display significant narrow

**Table 3**  
Mare Moscovienne FeO and TiO<sub>2</sub> Concentrations Obtained in the Present Study and Compared with Previously Published Results

	Regions	Present Study (M <sup>3</sup> )	Lucey et al. (2000) (Clementine— UV/VIS)	Lawrence et al. (2001) (LP)	Sato et al. (2017) (LROC-WAC)	Lemelin et al. (2019) (MI)
FeO	Mare material of dark plains	16%–20%	12%–18%	12%–18%	...	16%–20%
	Subdued craters	8%–16%	6%–14%	10%–15%	...	12%–16%
	Smooth and light plains	12%–16%	18%–20%	15%–18%	...	14%–18%
	Rolling terra	4%–8%	5%–8%	6%–8%	...	5%–9%
	Komarov crater (FFC)	12%–16%	10%–18%	16%–18%	...	16%–20%
TiO <sub>2</sub>	Mare material of dark plains	6%–8%	5%–7%	...	5%–9%	...
	Subdued craters	1%–4%	3%–4%	...	2%–4%	...
	Smooth and light plains	2%–4%	2%–4%	...	2%–5%	...
	Rolling terra	1%–2%	0%–2%	...	0%–2%	...
	Komarov crater (FFC)	4%–6%	4%–5%	...	3%–6%	...

asymmetrical absorption and moderate wide absorption toward 2000 nm (King & Ridley 1987; Cloutis & Gaffey 1993; Corley 2016; Arivazhagan & Karthi 2018). The spectral absorptions at 2  $\mu\text{m}$  IBD exhibit strong calcic pyroxene and low calcic pyroxene. The HCP shows strong narrow symmetrical absorption at 1000 nm and moderate absorption at 2100 nm. LCP shows strong asymmetrical absorption at 900 nm and broad absorption at 1850 nm (Figure 9(C)(iii)).

### 6.5. Chronological Study

Morota et al. (2009) studied part of the Mare Moscoviense chronology that was mapped with four regions using the SELENE - Terrain Camera (TC) through the CSFD method and identified that highland unit of the basin as  $\sim 4.1$  Ga. Moreover, it was also compared to the stratigraphy of Neukum et al. (2001), who applied the Nectarian system, and is consistent with the classification of Wilhelms et al. (1987). The oldest unit in the southern part was measured as 3.9 Ga and the northwestern unit's age was estimated as 3.5 Ga. The eastern unit's age of the mare basalt was estimated as 2.6 Ga. In addition, the author addressed the mare volcanism in Mare Moscoviense which was active until  $\sim 1.5$  Ga (Morota et al. 2009). Haruyama et al. (2009) recorded the ages of the southern and eastern units of Mare Moscoviense using SELENE-TC data. The CSFD of the northwestern unit yields a model age of 3.50 Ga, and the eastern unit is younger and has a model age of 2.57 Ga. It has been interpreted that the eastern unit is superposed on an older unit with age of 3.50 Ga.

In the present study, the Moscoviense basin has been divided into four different units as unit 1–4 based on the geological boundary data of the unified geologic map of the Moon (Fortezzo et al. 2020) (Figure 10(i)). The AMA plots are displayed in Figure 10(ii). Unit-1 shows the Imbrian age (3.65 Ga), which indicates the formation is younger than the Imbrium basin (3.85 Ga), but older than younger mare materials of the Moon (3.2–3.5 Ga) (Chao et al. 1973). Unit-2 gives the age of about 3.57 Ga, which comes under the middle Imbrian and represents the younger and intermediate mare deposition. Unit-3 features a high density of craters with an age of 3.8 Ga, indicating that this could be formed throughout the end of the Nectarian to the beginning of the Imbrian period. Unit-4 yields the age of about 3.92 Ga which comes under the Nectarian period.

## 6.6. Mineralogical Observations from Moscoviense Basin Features

### 6.6.1. Ray Crater

Ray crater has high maturity at the rim margin and low maturity in the middle (Figure 12(a)). The FeO composition of the ray crater ranges between 0% and 8%. (Figure 12(b)). The ray crater shows low TiO<sub>2</sub> concentration (1%–2%), as

illustrated in red and green in Figure 12(c). Figure 12(d) and (e) depicts the ray crater location map and M<sup>3</sup> spectral profiles collected from various regions of the ray crater respectively.

The orthopyroxene-olivine-spinel (OOS) lithology is represented by RC1 spectra, which exhibit modest orthopyroxene absorption near 890 nm, strong olivine absorption near 1050 nm and broad symmetrical spinel absorption near 2000 nm. Pieters et al. (2011) and Bhatt et al. (2018) discovered OOS and Mg-rich spinels in the Mare Moscoviense basin utilizing a unique wide absorption band at 2000 nm with Ch-1 M<sup>3</sup> data. Due to the obvious Fe<sup>2+</sup> location in a tetrahedral site, the spinel reflectance spectra exhibit a very significant electronic transition absorption at about 2000 nm. In contrast, the Mg-rich spinel contains minor Fe<sup>2+</sup> and is quite bright, but iron-rich chromites manifest several absorptions in the visible (500–1000 nm) area due to Fe<sup>2+</sup>, Cr<sup>2+</sup> and Cr<sup>3+</sup> transitions (Cloutis et al. 2004; Pieters et al. 2011). The RC2 and RC4 spectra show moderate Fe<sup>2+</sup> asymmetrical absorption near 730–850 nm, and strong asymmetric absorption between 970 and 990 nm, as well as broad asymmetric absorption between 2000 and 2100 nm due to clinopyroxene, weak plagioclase absorption at 1250 nm and moderate ilmenite absorption at 1489 nm, which correspond to the basaltic composition. The RC3 spectra indicate high asymmetrical olivine absorption at 1050 nm and strong wide CPx absorption at 2000 nm, which might be OPM. The noritic anorthosite is indicated by moderate Fe<sup>2+</sup> absorption at 850 nm, strong asymmetrical narrow plagioclase absorption around 1250 nm and moderate OPx wide asymmetrical absorption at 1900 nm in RC5 spectra. The orthopyroxene spectra reveal two large absorption bands about 900 nm (band 1) and 1900 nm (band 2), ascribed to crystal field transitions in Fe<sup>2+</sup>, which preferentially occupy the M2 crystallographic position (Adams 1974; Adams 1975; Cloutis & Gaffey 1991; Burns 1993; Cloutis 2002).

### 6.6.2. Wrinkle Ridge

The wrinkle ridge's OMAT shows low maturity (Figure 13(a)). The central and southern sections of the ridge have around 12% FeO content, whereas the northern half has moderate and low concentrations (Figure 13(b)). The wrinkle ridge has a TiO<sub>2</sub> concentration ranging  $>2\%$ . (Figure 13(c)). Figure 13 depicts the wrinkle ridge location map and M<sup>3</sup> spectral profiles taken from various portions of the wrinkle ridge (Figure 13(d) and (e)). The WR-1, WR-3 and WR-5 exhibit weak Fe<sup>2+</sup> absorptions between 750 and 890 nm, strong asymmetrical absorptions between 990 and 1010 nm, as well as strong broad asymmetrical absorptions between 2000 and 2137 nm due to CPx, moderate plagioclase absorptions near 1250 nm, and moderate and weak ilmenite absorptions between 1400 and 1470 nm, representing the basaltic composition. The WR-2 and WR-4 spectra exhibit mild Fe<sup>2+</sup> absorptions between 830–890 nm, significant narrow asymmetrical

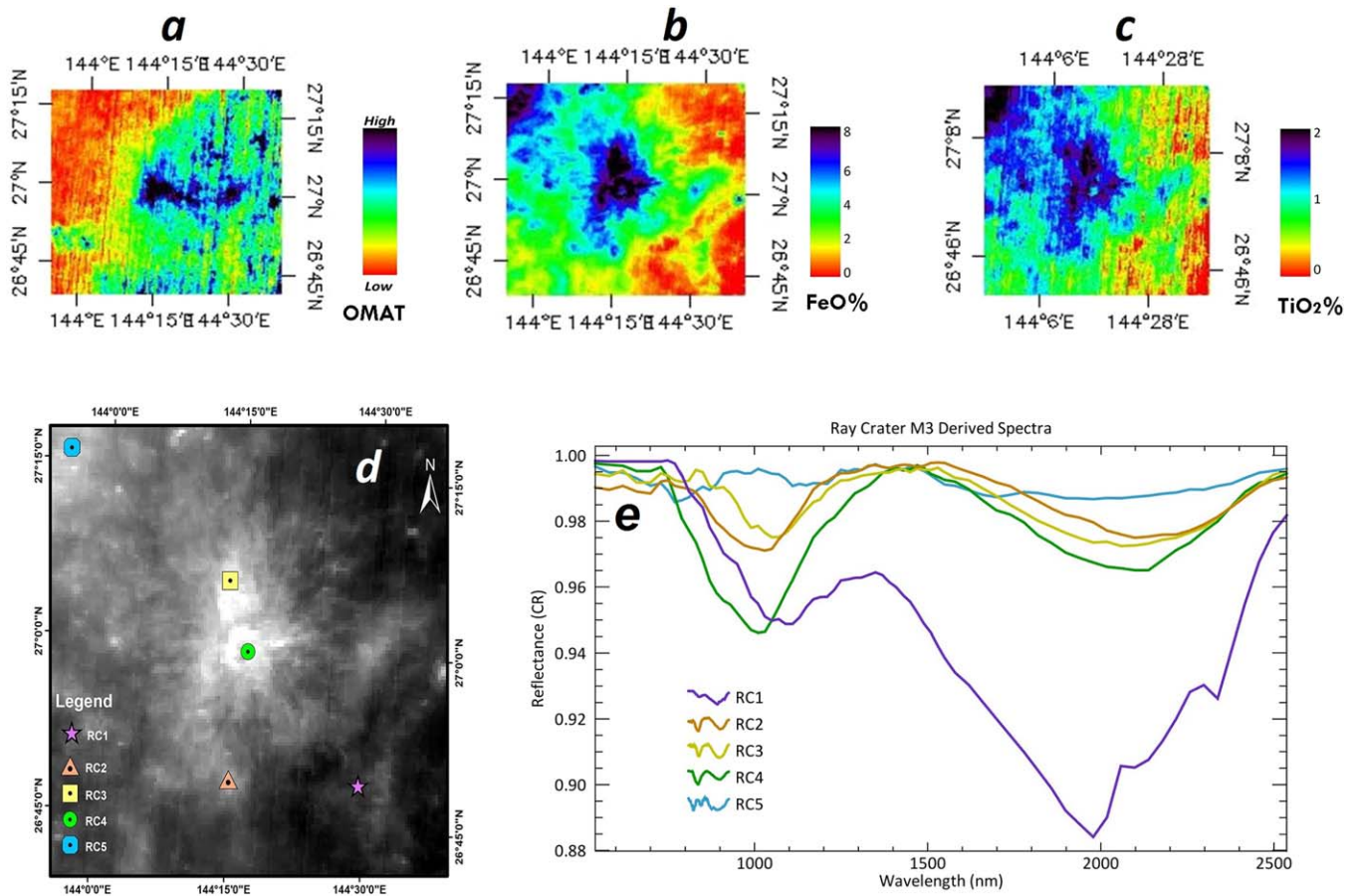


**Figure 12.** (a) Ray crater OMAT map. (b) Ray crater FeO map. (c) Ray crater TiO<sub>2</sub> map. (d) Location map of the ray crater. (e) Spectral information for ray crater (RC1-5) from M<sup>3</sup>.

absorptions between 990–1030 nm, and broad asymmetrical absorptions owing to CPx between 2058–2137 nm. Weak plagioclase absorption at 1289 nm indicates gabbroic composition.

### 6.6.3. Swirls

The eastern section of the swirls has low maturity and high maturity found in the other zones (Figure 14(a)). The swirls' FeO concentration ranges up to 9% (Figure 14(b)), while their TiO<sub>2</sub> content ranges >2% (Figure 14(c)). Figure 14 depicts the swirls location map and M<sup>3</sup> spectral profiles collected from various regions of the swirls (Figure 14(d) and (e)). The SW-1, SW-3 and SW-5 spectra indicate moderate Fe<sup>2+</sup> absorptions between 810 and 830 nm, strong asymmetrical CPx absorptions detected around 970 nm, as well as strong wide range asymmetric absorption seen between 2097 and 2137 nm due to CPx, weak olivine absorption observed at 1050 nm, weak and moderate plagioclase absorptions observed near 1250 nm, and moderate Ti-ilmenite absorption, representing the basaltic composition. SW-2 and SW-4 spectra reveal modest Fe<sup>2+</sup>

absorptions between 830 and 890 nm, strong narrow absorptions between 990 and 1030 nm, broad asymmetrical absorptions due to CPx between 2058–2137 nm, and weak plagioclase absorptions at 1289 nm, indicating a gabbroic composition.

### 6.6.4. Unnamed Craters (Suspected)

The OMAT of unnamed craters (suspected) demonstrates that the rim and southern regions of the craters are immature, but the outside portions of the craters are mature (Figure 15(a)). The unnamed (suspected) craters have FeO concentrations ranging up to 12%. The central and southern regions of the craters exhibited low FeO concentrations, whereas the western and eastern portions of the middle crater have moderate to high concentrations (Figure 15(b)). The TiO<sub>2</sub> content of the unnamed craters ranges >4%, with the southern (very low TiO<sub>2</sub>) and northern (low TiO<sub>2</sub>) parts having the highest concentrations (Figure 15(c)).

The unnamed crater's position map and M<sup>3</sup> spectral profiles derived from various regions of the unnamed crater are

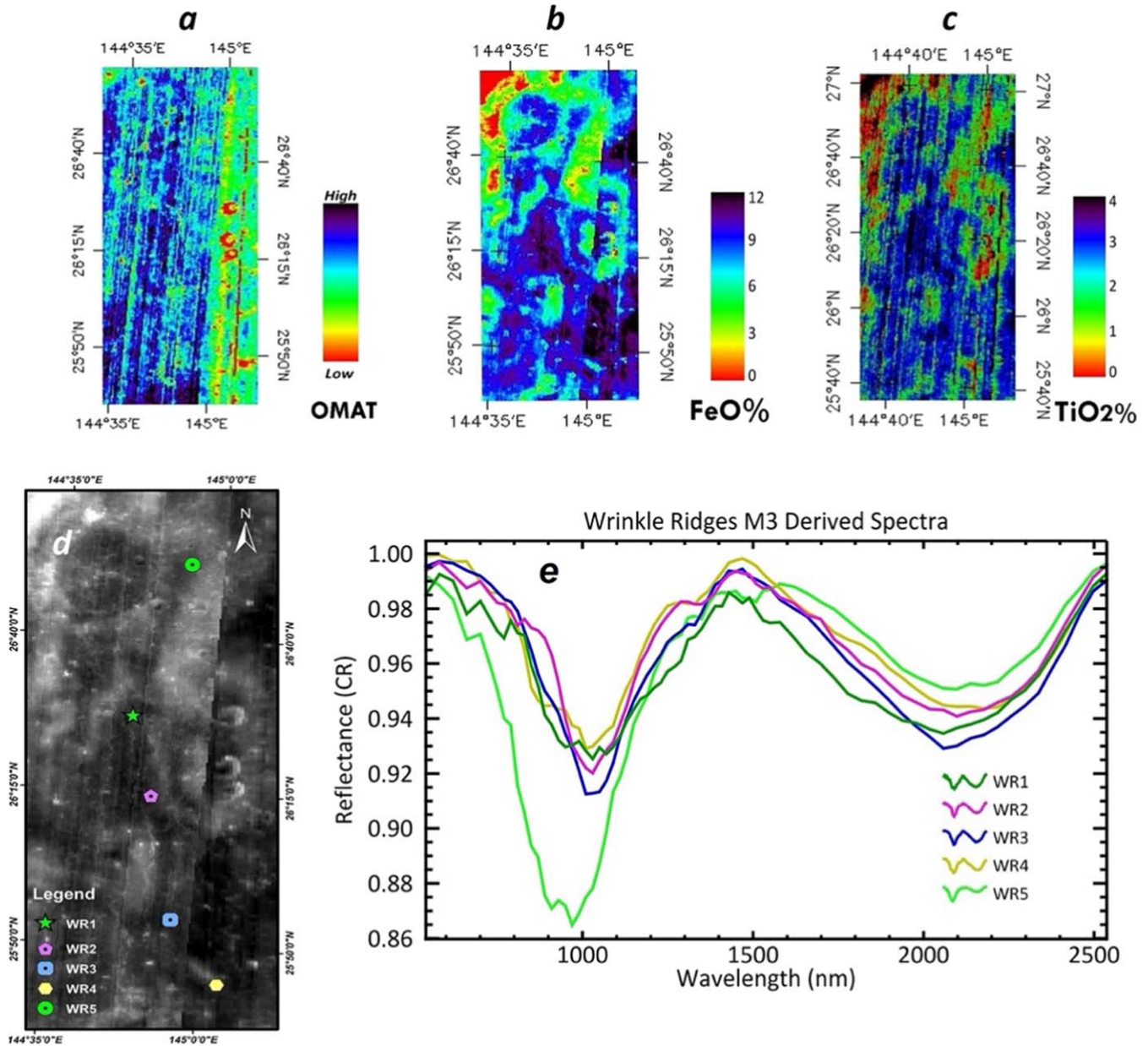


**Figure 13.** (a) Wrinkle ridge OMAT map. (b) Wrinkle ridge FeO map. (c) Wrinkle ridge TiO<sub>2</sub> map. (d) Location map of the wrinkle ridge. (e) Spectral information of wrinkle ridge (WC1-5) from M<sup>3</sup>.

displayed in Figure 15(d) and (e). UCS 1–5 spectra show weak Fe<sup>2+</sup> absorptions between 810 and 870 nm, strong asymmetrical CPx absorptions between 950 and 1010 nm, broad asymmetrical absorption between 2000 and 2177 nm, moderate plagioclase absorption near 1250 nm, and weak and moderate Ti-ilmenite absorptions in 1489–1548 nm, representing the basaltic composition. UCS-6 spectra display strong asymmetric plagioclase feldspar absorption near 1289 nm, as well as moderate asymmetrical ilmenite absorption noted at 1489 nm, indicating massive ilmenite (ilmenite + plagioclase) (40%–

50%). This may be generated from mafic component cumulates (noritic melt) (Anderson & Morin 1969; Amelin et al. 1994; Charlier et al. 2015).

According to compositional analyses, Ch-1 M<sup>3</sup> may be effectively utilized to map the principal minerals on the lunar surface such as pyroxene, olivine, plagioclase, ilmenite and spinel (Isacson et al. 2011; Klima et al. 2011; Mustard et al. 2011; Pieters et al. 2011; Lemelin et al. 2013; Corley 2016; Sivakumar et al. 2017). Pyroxene-bearing rocks were identified by absorption within 900–950 nm and 950–1010 nm, as well as

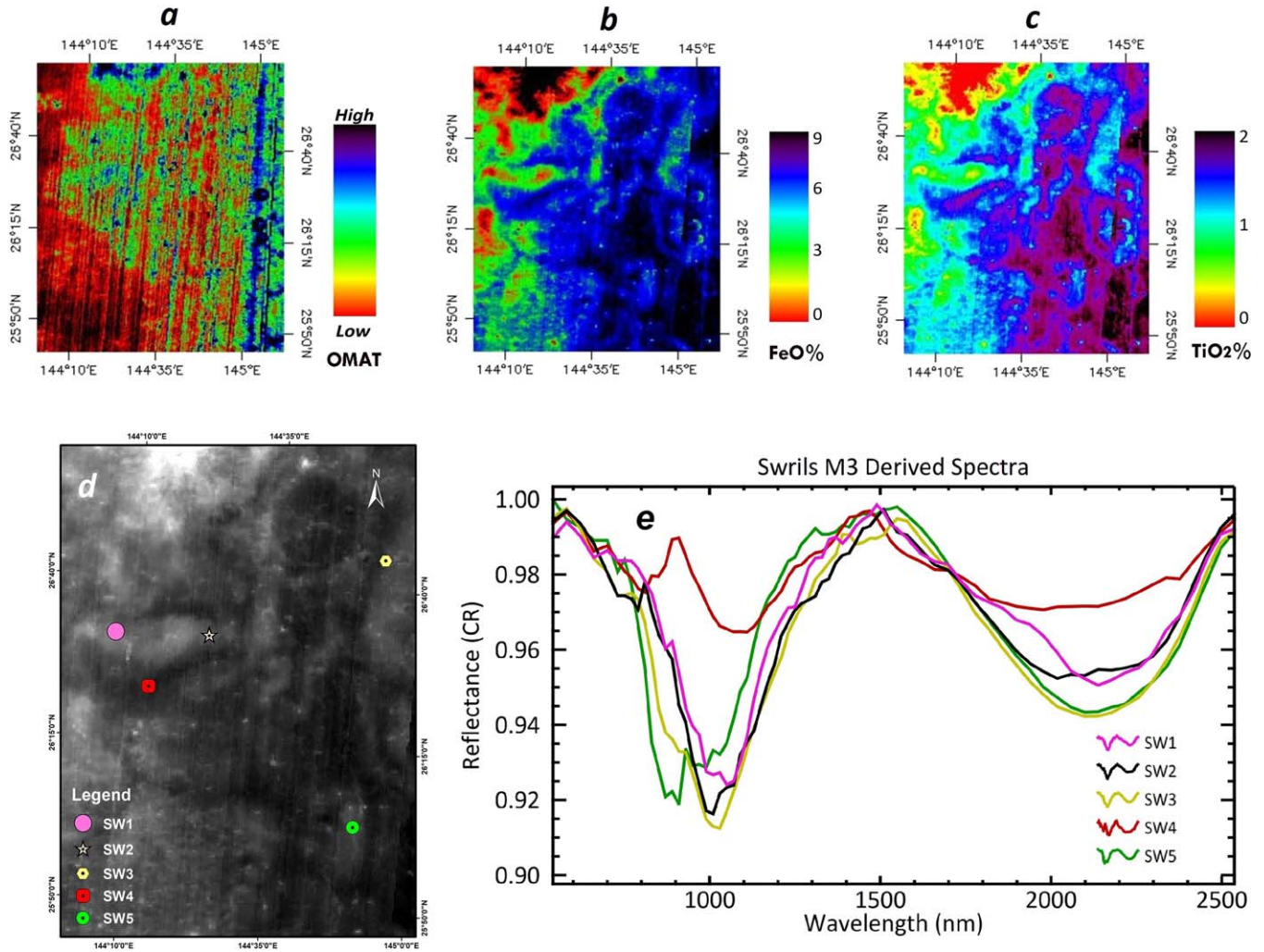


**Figure 14.** (a) Swirls OMAT map. (b) Swirls FeO map. (c) Swirls TiO<sub>2</sub> map. (d) Location map of the swirls. (e) Spectral information on swirls (SW1-5) from M<sup>3</sup>.

1850–1950 nm and 1950–2218 nm on the south side of the basin, wrinkle ridge, ray crater, swirls and unnamed craters, which may imply the presence of basaltic and gabbroic compositions. The olivine-pyroxene producing lithology is seen in the ray crater and swirling region through absorption at 1050 nm and between 2000 and 2137 nm, indicating a relatively thin crust and corresponding to olivine-pyroxene mixture rock (Corley 2016; Arivazhagan & Karthi 2018). The presence of mild and moderate plagioclase is detected by absorption at 1250 nm in the ray crater, wrinkle ridge, swirls and unnamed crater areas, indicating anorthositic composition and confirming the LMO concept (Papike et al. 1976). Ilmenite is the most abundant compositional variation in lunar mare basalts (low Ti–high Ti), which may show significant differences in mantle origins on the surface of the Moon (Adams & Goulaud 1978; Lemelin et al. 2013; Arivazhagan 2015; Sivakumar et al. 2017). The existence of ilmenite with

varying TiO<sub>2</sub> percent concentration was detected in the ray crater, wrinkle ridge, swirls and unnamed crater locations in the current investigation, indicating the presence of ilmenite with variable TiO<sub>2</sub> percent concentration. Strong absorption at 2000 nm is seen in the ray crater due to spinel (OOS) composition, indicating the formation of mantle (mare) components in the Mare Moscoviense basin (Pieters et al. 2011; Bhatt et al. 2018).

## 7. Conclusion

In the present study, we have used Ch-1 M<sup>3</sup> and LROC-WAC for compositional, chronological and topographical characterization of the Mare Moscoviense basin.

1. The inner basin mostly occupies the smooth mare plains, whereas rouged surface units are observed on the eastern side (surrounded by the Titov crater region). The basin

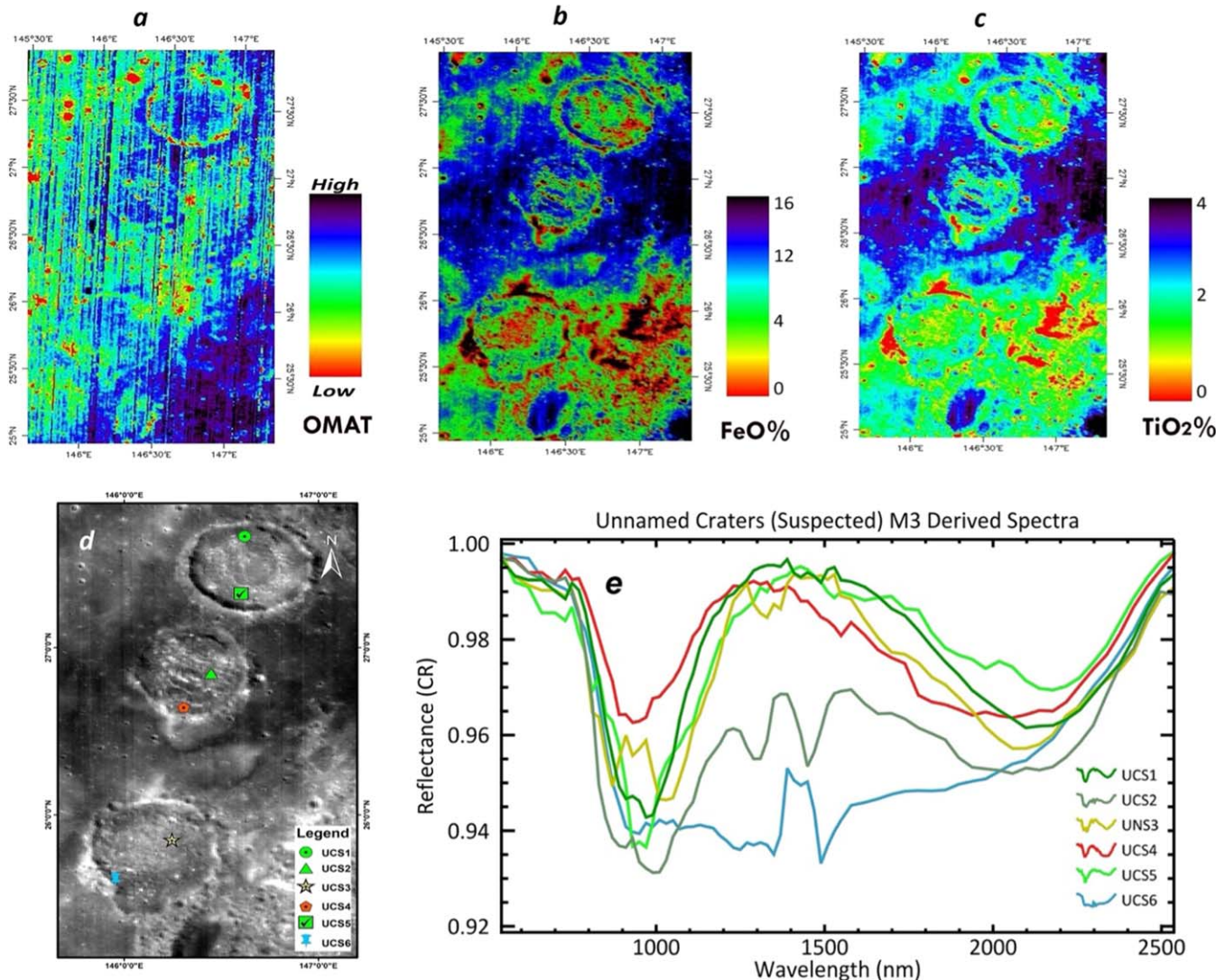


**Figure 15.** Unnamed craters. (a) OMAT map. (b) FeO map. (c) TiO<sub>2</sub> map. (d) Location map. (e) Spectral information (UCS1-6) from M<sup>3</sup>.

slopes have been observed as 0°–37°. The mare surface provinces show a low slope pattern (0%–10%), whereas the high slope pattern (25°–37°) is identified at the craters. The smooth mare surface provinces have a low slope pattern (0%–10%), whereas the high slope pattern is identified at the craters. Hence, it is revealed that the inner surface mare emplacement happened in the basin center, after which the major cratering activity had not occurred in the basin surface (in an action of intermediate age). Therefore, the mare basin materials are still smooth; however, the rugged units can be seen near the eastern part, indicating the older units on the surface.

2. The M<sup>3</sup> SBR approach is utilized for lithological discrimination of mature mare units, mafic units, mare material contamination with highland units, and highland

lithology and confirmed by the characterization of respective M<sup>3</sup> spectral absorption features.

- Using M<sup>3</sup> data, higher FeO concentration (up to 20%) is discovered in the southern section of the Mare Moscoviense basin. The presence of TiO<sub>2</sub> concentration is noted up to 8%. The Mare Moscoviense basin is primarily (spatially) covered by intermediate TiO<sub>2</sub> basalts (middle Imbrian aged formation) (4.5%–7.5% TiO<sub>2</sub>) with ages ranging from 3.5 Ga to 3.6 Ga, which might have formed from olivine-ilmenite-pyroxene cumulates at depths ranging from 200 to 500 km.
- 1 μm & 2 μm IBD indicates the existence of mineral compositions such as ortho and clinopyroxenes (central and southern parts), olivine (northwest region near ray crater) and olivine-pyroxene mixtures (southern edge of

the basin). The occurrence of olivine and olivine-pyroxene combinations might indicate that the Mare Moscoviense basin has a relatively shallow crust.

5. According to the LROC-WAC CSFD chronological investigations, the basin mare units have ages of 3.57 Ga (unit-2) and 3.65 Ga (unit-1), whereas other units have ages of 3.8 Ga (unit-3) and 3.92 Ga (unit-4). The basin's primary activity occurred between 3.4 Ga and 3.9 Ga (Imbrian-Nectarian period impact cratering and mare emplacement). The regions of U-3 and U-4 show the Nectarian age, which could indicate the primordial unit deposit accumulated in the basin-like anorthositic contamination (e.g., Titov crater ejecta), which is also observed and validated from the SBR map. The U-1 and U-2 exhibit the middle Imbrian age, which indicates that they are entirely filled by the mare units, according to the TiO<sub>2</sub> map, illustrating the dominance of intermediate basalt that occurred in the basin.
6. The ortho and clinopyroxenes, olivine, OPM, plagioclase, ilmenite and spinel (OOS) compositions were revealed by the M<sup>3</sup> reflectance spectral characterization, indicating the presence of basaltic, anorthositic, gabbroic and ilmenite rock types in the Mare Moscoviense basin.
7. The Chandrayaan-2 orbiter, which may give higher spatial and spectral resolution data, can be used for the quantitative mineral/elemental abundance mapping. Future in situ/sample return missions can be planned to better understand the Moscoviense basin.

### Acknowledgments

The authors would like to acknowledge the Indian Space Research Organization, Bangalore, for funding under the Ch-1 AO Research Project (ISRO/SSPO/CH-1/2016–2019) to carry out this research work.

### References

- Adams, J. B. 1974, *JGR*, **79**, 4829
- Adams, J. B. 1975, in *Infrared and Raman Spectroscopy of Lunar and Terrestrial Minerals*, ed. C. Karr., Jr. (New York: Academic), 91
- Adams, J. B., & Goullaud, L. H. 1978, *LPSC*, **9**, 1
- Aharonson, O., Zuber, M. T., & Rothman, D. H. 2001, *JGR*, **106**, 23723
- Allen, C. C., Bond, G. G., & McKay, D. S. 1994, *Engineering, Construction and Operations in Space IV*, American Society of Civil Engineering
- Amelin, Y. V., Heaman, L. M., Verchogliad, V. M., & Skobelev, V. M. 1994, *COMP*, **116**, 411
- Anbazhagan, S., & Arivazhagan, S. 2009, *P&SS*, **57**, 1346
- Anderson, A. T., & Morin, M. 1969, in *Origin of Anorthosite and Related Rocks*, ed. Y. W. Isachsen (NY: State Mus Sci Serv Mem), 57
- Arivazhagan, S., & Anbazhagan, S. 2012, *Lithological discrimination of Apollo 17 landing site using chandrayaan1 Moon mineralogical mapper data*, 43rd Lunar and Planetary Science Conference, #1751
- Arivazhagan, S. 2015, in *Planetary Exploration and Science: Recent Results and Advances*, ed. S. Jin et al. (Berlin: Springer Geophysics), 21
- Arivazhagan, S., & Karthi, A. 2018, *P&SS*, **161**, 41
- Atheer, L. S., Mühlbauera, M., Grumpea, A., et al. 2016, *The International Archives of the Photogrammetry, Remote Sensing and Spatial Information Sciences*, Volume XLI-B4, 479
- Bharti, R., Ramakrishnan, & Dand Singh, K. D. 2014, *JESS*, **123**, 233
- Bhatt, M., Wöhler, C., Dhingra, D., et al. 2018, *Icar*, **303**, 149
- Blewett, D. T., Coman, E. I., Hawke, B. R., et al. 2011, *JGRE*, **116**, 30
- Blewett, D. T., Lucey, P. G., Hawke, B. R., & Jolliff, B. L. 1997, *JGR*, **102**, 16,319
- Burns, R. G. 1993, *Mineralogical Applications of Crystal Field Theory*, Vol. 5 (2nd edn.; Cambridge: Cambridge Univ. Press), 220
- Calzada, A., & Mest, S. C. 2013, *Scientific Characterization of Mare Moscoviense Region of Interest*, European Planetary Science Congress Abstracts, 8, 167
- Chao, E. C. T., Soberblom, L. A., Boyce, J. M., Wihelms, D. E., & Hodegs, C. A. 1973, *Lunar Light Plains Deposits*, Lunar Planetary Science Institute
- Charette, M. P., Thomas, B. M., & Carle, P. 1974, *JGR*, **79**, 1605
- Charlier, B., Namur, O., Bolle, O., Latypov, R., & Duchesne, J.-C. 2015, *ESRv*, **141**, 56
- Cloutis, E. A. 2002, *JGRE*, **107**, 5039
- Cloutis, E. A., & Gaffey, M. J. 1991, *JGRE*, **96**, 22809
- Cloutis, E. A., & Gaffey, M. J. 1993, *Icar*, **102**, 203
- Cloutis, E. A., Sunshine, J. M., & Morris, R. V. 2004, *M&PS*, **39**, 545
- Corley, M. L. 2016, *Lunar olivine Exposures: Origins and mechanisms of transport*, Final Report, University of Hawaii submitted
- Craddock, R. A., Robinson, M. S., Hawke, B. R., & McEwen, A. S. 1997, *Lunar and Planetary Science XXVIII* #1499.3
- Crown, D. A., & Pieters, C. M. 1987, *Icar*, **72**, 492
- Dowty, E. 1975, *Shallow Origin of mare Basalts*. Conf. on Origins of mare Basalts, **234**, 35
- Elardo, S. M., Draper, D. S., & Shearer, C. K. 2011, *GeCoA*, **75**, 3024
- Fortezzo, et al. 2020, 51st Lunar and Planetary Science Conference #2760
- Giguere, T., Taylor, G. J., Hawke, B. R., & Lucey, P. G. 2000, *M&PS*, **35**, 193
- Gillis, J. J. 1998, Ph.D. thesis, Rice Univ., Houston, Tex. 248
- Goswami, J. N., & Annadurai, M. 2009, *Lunar Planetary Science (CDROM)*, **40**, 2571
- Grier, J. A., McEwen, A. S., Lucey, P. G., Milazzo, M., & Strom, R. G. 2001, *JGR*, **106**, 32,847
- Haruyama, J., Ohtake, M., Matsunaga, T., et al. 2009, *Sci*, **323**, 905
- Head, J. W. 1976, *RvGeo*, **14**, 265
- Herbert, F. 1980, Proc. 11th Lunar Planet. Sci. Conf., 2015
- Hess, M., Wohlfarth, K., Wöhler, C., et al. 2020, EPSC Abstracts, 14, EPSC2020-716
- Hess, P. 1991, *Geophys. Res. Lett*, **18**, 2069
- Hess, P., & Parmentier, M. 1995, *Earth Planet. Sci. Lett.*, **134**, 501
- Howari, F. M., Sharma, M., Xavier, C. M., Nazzal, Y., & AlAydarooos, F. 2021, *Front. Environ. Sci.*, **9**, 605893
- Howari, F. M., Sharma, M., Xavier, C. M., Nazzal, Y., & Alaydarooos, F. 2022, *FrASS*, **8**, 1
- Isaacson, P. J., Petro, N. E., Pieters, C. M., et al. 2013, *JGRE*, **118**, 369
- Isaacson, P. J., Pieters, C. M., Sebastien, B., et al. 2011, *JGRE*, **116**, E00G11
- Jaumann, R., Hiesinger, H., Anand, M., et al. 2012, *P&SS*, **74**, 15
- Jin, S., Arivazhagan, S., & Araki, H. 2013, *AdSpR*, **52**, 285
- Jolliff, B. L. 2006, *New Views of the Moon*, Miner. Soc. Of Am., Chantilly, Va., 721
- Karthi, A., & Arivazhagan, S. 2022, *Icaru*, **375**, 114844
- King, T. V. V., & Ridley, W. I. 1987, *JGR*, **92**, 11,457
- Klima, R. L., Pieters, M. C., Joseph, W. B., et al. 2011, *JGRE*, **116**, E00G06
- Kneissl, T., Van Gasselt, S., & Neukum, G. 2011, *P&SS*, **59**, 1243
- Kramer, G. Y., Besse, S., Nettles, J., et al. 2011, *JGRE*, **116**, E6
- Kreslavsky, M. A., & Head, J. W. 1999, *JGR*, **104**, 21911
- Kreslavsky, M. A., & Head, J. W. 2016, *Icar*, **273**, 329
- Kumar, A. S., Roy Chowdhury, A., Banerjee, A., et al. 2009, *CSci*, **96**, 496
- Lawrence, D. J., Feldman, W. C., Elphic, R. C., et al. 2001, in 32nd LPSC
- Le Mouélic, S. 2001, *P&SS*, **49**, 65
- Lemelin, M., Lucey, P. G., Miljkovic, K., et al. 2019, *PSS*, **165**, 230
- Lemelin, M., Morisset, E. E., Germain, M., et al. 2013, *JGRE*, **118**, 2582
- Ling, Z. C., Zhang, J., Liu, J. Z., et al. 2011, *ChSBu*, **56**, 2082
- Longhi, J. 1992, *Geochim. Cosmochim. Acta*, **56**, 2235

- Lucey, P. G., Blewett, D. T., Johnson, J. L., Taylor, G. J., & Hawke, B. R. 1996, *Lunar Planet Sci*, **27**, 781
- Lucey, P. G., Blewett, D. T., & Jolliff, B. L. 2000a, *JGR*, **105**, 20,297
- Lucey, P. G., Blewett, D. T., Taylor, G. J., & Hawke, B. R. 2000b, *JGR*, **105**, 20,377
- Lucey, P. G., Jennifer, D. T., & Hawke, B. R. 1998, *JGR*, **103**, 3679
- Lunar swirls, [https://wms.lroc.asu.edu/lroc/view\\_rdr/SHAPEFILE\\_LUNAR\\_SWIRLS](https://wms.lroc.asu.edu/lroc/view_rdr/SHAPEFILE_LUNAR_SWIRLS) (Website I)
- Lunar Wrinkle Ridge., [https://wms.lroc.asu.edu/lroc/view\\_rdr/SHAPEFILE\\_WRINKLE\\_RIDGES](https://wms.lroc.asu.edu/lroc/view_rdr/SHAPEFILE_WRINKLE_RIDGES). (Website II)
- Meng, Z., Chen, W., Wang, Z., et al. 2020, *RemS*, **12**, 535
- Michael, G. G., & Neukum, G. 2010, *Earth and Plan Sci Let*, **294**, 223
- Mikolajewski, S., Hiesinger, H., van der Bogert, C. H., & Schmedemann, N. 2021, Landing Site Evaluation Inside Mare Moscoviense. 52nd Lunar and Planetary Science Conference 2021 (LPI Contrib. No. 2548), #2087
- Morota, T., Haruyama, J., Honda, C., et al. 2009, *GeoRL*, **36**
- Mustard, J. F., Pieters, C. M., Isaacson, P. J., et al. 2011, *JGRE*, **116**, E00G12
- Neukum, G., Ivanov, B. A., & Hartmann, W. K. 2001, *SSRv*, **96**, 55
- Ouyang, Z. Y. 2005, Introduction to Lunar Science (Beijing: China Space Press)
- Ouyang, Z. Y., Li, C., Zhang, H., et al. 2010, *Sci. China Earth Sci*, **53**, 1565
- Papike, J. J., Hodge, F. N., Bence, A. E., Cameron, M., & Rhode, J. M. 1976, *Rev. Geophys. Space Physics*, **14**, 475
- Pieters, C. M., Besse, S., Boardman, J., et al. 2011, *JGRE*, **116**, E00G08
- Pieters, C. M., & Englert, P. A. 1997, Remote Geochemical Analysis: Elemental and Mineralogical Composition (New York: Cambridge Univ. Press), 312
- Pike, R. J., & Spudis, P. D. 1987, Basin-ring Spacing on the Moon, Mercury, and Mars, *Earth Moon Planets*, **39**, 129
- Qiao, L., Chen, J., Xu, L., et al. 2021b, *Icar*, **364**, 114480
- Qiao, L., Head, J. W., Wilson, L., Chen, J., & Ling, Z. 2021a, *JGRE*, **126**, e2021JE0068
- Qiao, L., Xiao, L., Zhao, J., Huang, Q., & Haruyama, J. 2014, *P&SS*, **101**, 37
- Qiao, L., Xu, L., Yang, Y., et al. 2021c, *GeoRL*, **48**, e2021GL095132
- Reiner, M. A., Lucey, P. G., Desch, S. J., & McCubbin, F. M. 2009, *GeoRL*, **36**, L02201
- Richmond, N. C., Hood, L. L., Mitchell, D. L., et al. 2005, *JGR*, **110**, E05011
- Robinson, M. S., Brylow, S. M., Tschimmel, M., et al. 2010, *SSRv*, **150**, 81
- Robbins, S. J. 2018, *JGRE*, **124**, 871
- Robbins, S. J. 2016, Developing a Global Lunar Crater Database, complete for craters for craters  $\geq 1$  km. LPSC XXXXVII, abstract #1525
- Rosenburg, M. A., Aharonson, O., Head, J. W., et al. 2011, *JGRE*, **116**, E02001
- Ryder, G. 1991, *GeoRL*, **18**, 2065
- Salem, I. B., Sharma, M., Kumaresan, P. R., et al. 2022, *RemS*, **14**, 814
- Sato, H., Robinson, M. S., Lawrence, S. J., et al. 2017, *Icar*, **296**, 216
- Sharpton, V. L., & Head, J. W. 1985, *JGR*, **90**, 3733
- Shearer, C. K., & Papike, J. J. 1999, *AmMin*, **84**, 1469
- Shearer, C. K., & Papike, J. J. 2005, *GeCoA*, **69**, 3445
- Shearer, C. K., Hess, P. C., Wieczorek, M. A., et al. 2006, *RvMG*, **60**, 365
- Sivakumar, R., Neelakantan, R., & Santosh, M. 2017, *Geoscience Frontiers*, **8**, 457
- Smith, J. V., Anderson, A. T., Newton, R. C., et al. 1970, in Proc. Apollo 11 Lunar Sci. Conf, **1**, 897
- Snyder, G. A., Taylor, L. A., & Neal, C. R. 1992, *GeCoA*, **56**, 3809
- Stepinski, T. F., Ding, W., & Vilalta, R. 2012, Intelligent Data Analysis for Real-Life Applications: Theory and Practice (Hershey, PA: IGI Global), 146
- Stoffler, D., Ryder, G., Ivanov Boris, A., et al. 2006, *RvMG*, **60**, 519
- Thaisen, K. G., Head, J. W., Taylor, L. A., et al. 2011, *JGRE*, **116**, E00G07
- Unified Geologic Map of the Moon (1:5M) (2020), [https://astrogeology.usgs.gov/search/map/Moon/Geology/Unified\\_Geologic\\_Map\\_of\\_the\\_Moon\\_GIS](https://astrogeology.usgs.gov/search/map/Moon/Geology/Unified_Geologic_Map_of_the_Moon_GIS).
- Warren, P. H. 1985, *Annu. Rev. Earth Planet. Sci.*, **13**, 201
- Wilhelms, D. E., McCauley, J. F., & Trask, N. J. 1987, The Geologic History of the Moon (Washington, DC: U.S. Geol. Surv.), 302
- Wood, J. A., Dickey, J. S., Marvin, U. B., & Powell, B. N. 1970, Proc. Apollo 11 Lunar Sci. Conf., **1**, 965
- Wu, Y., Bin, X., Zhao, B., et al. 2012, *JGR*, **117**, E02001
- Yue, Z., Michael, G. G., Di, K., & Liu, J. 2017, *Earth Planet. Sci. Lett.*, **477**, 14
- Zhang, W., Hu, J., & Yu, H. 2020, Lunar Subsurface Mineralogy and Density Profile Modelling based on Moon Mineralogy Mapper Observation. *Acta Geologica Sinica—English Edition*, **10.1111/1755-6724.14511**